

On the choice and implications of rheologies that maintain kinematic and dynamic consistency over the entire earthquake cycle

Rishav Mallick¹, Valere Lambert¹, and Brendan J Meade²

¹California Institute of Technology

²Harvard University

November 24, 2022

Abstract

Viscoelastic processes in the upper mantle redistribute seismically generated stresses and modulate crustal deformation throughout the earthquake cycle. Geodetic observations of these motions at the Earth's surface offer the possibility of constraining the rheology of the upper mantle. Parsimonious representations of viscoelastically modulated deformation should simultaneously be able to explain geodetic observations of rapid postseismic deformation and near-fault strain localization late in the earthquake cycle. We compare predictions from time-dependent forward models of deformation over the entire earthquake cycle on and surrounding an idealized vertical strike-slip fault in a homogeneous elastic crust underlain by a homogeneous viscoelastic upper mantle. We explore three different rheologies as inferred from laboratory experiments: 1) linear-Maxwell, 2) linear-Burgers, 3) power-law. Both the linear Burgers and power-law rheological models can be made consistent with fast and slow deformation phenomenology from across the entire earthquake cycle, while the single-layer linear Maxwell model cannot. The kinematic similarity of linear Burgers and power-law models suggests that geodetic observations alone are insufficient to distinguish between them, but indicate that one may serve as a proxy for the other. However, the power-law rheology model displays a postseismic response that is strongly earthquake magnitude dependent, which may offer a partial explanation for observations of limited postseismic deformation near magnitude 6.5-7.0 earthquakes. We discuss the role of mechanical coupling between frictional slip and viscous creep in controlling the time-dependence of regional stress transfer following large earthquakes and how this may affect the seismic hazard and risk to communities living close to fault networks.

On the choice and implications of rheologies that maintain kinematic and dynamic consistency over the entire earthquake cycle

Rishav Mallick^{1,2}, Valère Lambert³, and Brendan Meade⁴

¹Seismological Laboratory, California Institute of Technology

²Earth Observatory of Singapore, Nanyang Technological University, Singapore

³Seismological Laboratory, University of California, Santa Cruz

⁴Department of Earth and Planetary Sciences, Harvard University

April 28, 2022

Abstract

1
2 Viscoelastic processes in the upper mantle redistribute seismically generated stresses and
3 modulate crustal deformation rates throughout the earthquake cycle. Geodetic observations
4 of these motions at the surface of the coupled crust-mantle system offer the possibility of con-
5 straining the rheology of the upper mantle and the rates of stress transfer during the intervals
6 between large earthquakes. Parsimonious representations of viscoelastically modulated defor-
7 mation through the aseismic phase of the earthquake cycle should be able to simultaneously
8 explain decadal-scale geodetic observations of both rapid postseismic deformation and late in
9 the earthquake cycle near-fault strain localization. To understand how a choice of rheological
10 formulation affects kinematics, we compare predictions from time-dependent forward mod-
11 els of deformation over the entire earthquake cycle on and surrounding an idealized vertical
12 strike-slip fault in a homogeneous elastic crust underlain by a homogeneous viscoelastic up-
13 per mantle. We explore three different rheologies as inferred from laboratory experiments: 1)
14 linear Maxwell, 2) linear Burgers, and 3) power-law. Both the linear Burgers and power-law
15 rheological models can be made consistent with fast and slow deformation phenomenology
16 from across the entire earthquake cycle, while the single-layer linear Maxwell model cannot.
17 The kinematic similarity of both linear Burgers and power-law rheology models suggests that
18 geodetic observations alone may be insufficient to distinguish between these two rheologies,
19 but do indicate that one may serve as an effective proxy for the other. Additionally, the power-
20 law rheology model displays a postseismic response that is strongly earthquake magnitude
21 dependent, which may offer a partial explanation for observations of limited postseismic de-
22 formation near some magnitude 6.5-7.0 earthquakes. We discuss the role of mechanical cou-
23 pling between frictional slip and viscous creep in controlling the time-dependence of regional
24 stress transfer following large earthquakes and how this may affect the seismic hazard and risk
25 to communities living close to fault networks.

26 Plain Language Summary

27 The solid Earth is a viscoelastic material that displays both solid and fluid-like behaviors depend-
28 ing on the observational time window and the applied stress. We develop numerical simula-
29 tions of how the uppermost solid Earth responds to a sequence of periodic earthquakes and the
30 earthquake cycle. Our simulations test a range of proposed viscoelastic materials. The predicted
31 surface displacements from each model are compared with observational features extracted from
32 geodetic datasets compiled over the past few decades. All existing viscoelastic material descrip-
33 tions can satisfactorily explain observational features in the first few years following an earth-
34 quake; significant differences between the viscoelastic models emerge 10 - 100 years following a
35 large earthquake. Identifying the most appropriate viscoelastic description requires the integra-
36 tion of geodetic data that constrains the velocity evolution from a sequence of earthquakes (as
37 opposed to a single event) with observations from rock physics laboratory experiments. A uni-
38 fied description of viscoelasticity in the upper most solid earth has important implications for
39 understanding stress evolution in fault networks, and improving models of seismic hazard.

40 1 Introduction

41 Inferring the constitutive relations that describe how the macroscopic stress state of the lithosphere-
42 asthenosphere system evolves as a function of strain rate, total strain and intensive system vari-
43 ables (temperature, pressure, composition, etc.) remains a grand challenge in the geosciences
44 [NSF, 2020]. Constraining these constitutive relations, or rheology, is fundamental to our under-
45 standing of the dynamics of the solid Earth. From the occurrence of earthquakes and their effects
46 at any point within the Earth, to the construction of the geological structure that surrounds us and
47 the sustenance of plate tectonics itself, the rheology and strength of Earth materials plays a cru-
48 cial role in defining these processes [Bürgmann and Dresen, 2008; Mulyukova and Bercovici, 2019].
49 However, inferring these constitutive relations at the length scale of geological processes (> 1
50 kilometer) is a difficult task as aspects of rock failure are shown to be scale-dependent [e.g., Ya-
51 mashita et al., 2015; Lambert et al., 2021] and there are limited opportunities to conduct experiments
52 at the crustal or lithospheric scale. Our goal in this article is to demonstrate that the earthquake
53 cycle, in the vicinity of a mature strike-slip fault, may provide us with the necessary experimental
54 conditions to probe the rheology of the lithosphere.

55 While there exist a number of studies that have sought to infer rheological properties of Earth's
56 lithosphere-asthenosphere system using observations from the earthquake cycle [Bürgmann and
57 Dresen, 2008, and references therein], the interpretation of results from different methodologies for
58 extracting rheological parameters can be limited or challenged by three key assumptions. First, a
59 common approach to modeling geophysical systems is to prescribe a functional form of the rhe-
60 ological model a priori and then estimate the associated best-fitting set of rheological parameters
61 for that selected model, potentially with limited consideration of alternative rheological models
62 that may be equally or better supported by the observations. Second, studies are often limited to a
63 specific observational time window, such as a few years following an earthquake, from which the
64 aforementioned best-fit model parameters are estimated. As such, inferred parameters are tied to
65 the observational window that is probed, which may in part explain vastly different rheological
66 estimates determined for studies of the lithosphere over different observational windows [e.g.,
67 Pollitz, 2005, 2019; Ryder et al., 2007; Henriquet et al., 2019; Tamisiea et al., 2007; Milne et al., 2001;
68 Hussain et al., 2018; Larsen et al., 2005; Kaufmann and Amelung, 2000]. Finally, a common assump-
69 tion when processing observed time series is that the signal can be well-separated into a set of

70 linearly superimposed functions, thereby neglecting nonlinear interactions among the associated
71 physical processes.

72 In this work, we seek to develop a framework that overcomes some of these limitations and
73 can reconcile rheological inferences from different observational windows. As a starting point,
74 we focus on major observational features in geodetic time series obtained from mature strike-
75 slip fault settings globally, from immediately following earthquakes (postseismic period) to late
76 in the earthquake cycle (interseismic period). We do not attempt to directly optimize the fit to
77 data, rather we consider the generality and descriptive power of popular rheological models of
78 the lithosphere and study where each model can explain major observational features or is in-
79 sufficient [Tarantola, 2006]. To assist the reader with appreciating the task at hand, we begin by
80 providing some background on common rheological models that are used to describe lithospheric
81 deformation, general observational constraints available from geodesy and prevalent modeling
82 strategies in the literature.

83 1.1 Elasticity, friction and viscous creep

84 The rheology of the lithosphere does not appear to follow a single simple description at all timescales.
85 For example, the passage of seismic waves and the static displacement or deformation of Earth's
86 lithosphere in response to an earthquake tell us that the lithosphere can be described as an elas-
87 tic body over timescales ranging from seconds to a day. However, the entire lithosphere cannot
88 be elastic since the earthquake source itself is an inelastic process, generally considered to be a
89 frictional rupture restricted to a narrow shear band [Kanamori and Brodsky, 2004].

90 At timescales longer than a day, time-dependent deformation patterns of the solid Earth's sur-
91 face following large earthquakes is routinely imaged using geodetic and remote sensing observa-
92 tional techniques [Avouac, 2015]. These datasets reveal the non-elastic nature of the lithosphere
93 i.e., deformation that continues well after the initial source of deformation has ceased.

94 This observed time-dependent post-seismic deformation is thought to result from a combina-
95 tion of two different processes: (1) time-dependent frictional slip on fault planes (afterslip) while
96 the surrounding medium is elastic, and (2) time-dependent deformation of the entire medium
97 itself. Afterslip is thought to be limited to depths where frictional processes are mechanically
98 favourable and is typically modelled as $\sigma \propto \log(\dot{\epsilon})$, where $\dot{\epsilon}$ is the strain rate, σ is stress in the
99 body [Marone *et al.*, 1991]. Beyond this domain, distributed deformation of rocks in the form of
100 Newtonian and power-law processes are thought to dominate deformation styles [Montési, 2004;
101 Hirth and Kohlstedt, 2003]. Distributed deformation of the medium is commonly thought to be
102 a viscoelastic process where the short timescale stress perturbations are accommodated by the
103 elasticity of the medium ($\epsilon \propto \sigma$) while relaxation following instantaneous stress steps or long
104 timescale observations highlight the viscous properties of the medium i.e., $\dot{\epsilon} \propto \sigma^n$ (ϵ - strain, $\dot{\epsilon}$ -
105 strain rate, n - power exponent, σ - stress) [Karato *et al.*, 1986]. Laboratory experiments also suggest
106 that viscous flow laws exhibit unsteady or transient deformation i.e., the relationship between σ
107 and $\dot{\epsilon}$ is unique once steady state is achieved, which requires a finite amount of strain or time
108 [Post, 1977]. This style of deformation is often modeled using a Burgers rheology [e.g., Müller,
109 1986; Hetland and Hager, 2005].

110 1.2 Geodetic observations

111 Over the last three decades, space-based geodetic observations have provided direct observations
112 of deformation throughout the earthquake cycle. As a result, tectonic processes associated with

113 the preseismic and postseismic timescales are well imaged, and we derive and discuss only the
114 major features from these observations. In this study, we focus on mature strike-slip faults and
115 simplify them to a two-dimensional geometry and describe the characteristics of the interseismic
116 and postseismic period as imaged by geodetic techniques - the interseismic locking depth, the
117 postseismic relaxation time and cumulative postseismic deformation over a given time window.
118 These are key features that numerical models of the earthquake cycles along such faults attempt
119 to explain.

120 1.2.1 Interseismic observations

121 In between earthquakes, geodetic time series from most mature strike-slip fault settings appear
122 nearly linear in time, at least over available observational timescales (1-2 decades), and the esti-
123 mated velocities follow an S-shaped function in space, commonly modeled using the \tan^{-1} op-
124 erator (Figure 1) [e.g., *Vernant, 2015; Savage and Burford, 1973*]. Deviations from this expected
125 behavior do appear in the data, such as non-linearities in the time series and deviations from the
126 \tan^{-1} shape function, however these differences are mostly due to localized creep episodes (in
127 time and space) or time-invariant creep on some sections of the fault.

128 Geodetic velocities are typically fit well with the functional form $\frac{v^\infty}{\pi} \tan^{-1} \left(\frac{x}{x_d} \right)$, where v^∞ is the
129 estimated long-term slip rate on the fault and D_{lock} is the depth to which the fault is locked; beyond
130 this depth, the entire fault is assumed to creep along an infinitesimally narrow shear surface at
131 a time-invariant rate of v^∞ . Studies show that v^∞ estimates for major strike-faults globally match
132 the estimated geological slip rates of the same faults within measurement uncertainties [*Meade*
133 *et al., 2013*]. The estimated locking depth from this kind of modeling is on the order of 10 – 20
134 km, which is comparable to the thickness of the lithosphere over which frictional processes are
135 thought to be dominant [*Vernant, 2015*].

136 1.2.2 Postseismic observations

137 Following large earthquakes, time-dependent deformation occurs in the near-field as well as far
138 away from the fault. This time-dependent signal is typically decomposed into a linear term and a
139 decaying curvature term, i.e., a monotonic function that is bounded between 0 and its maximum
140 value (Figure 1). The linear term is assumed to represent background loading due to the motion
141 of tectonic plates. The curvature in the timeseries is typically fit with functional forms such as
142 $\log(t/t_R + 1)$ and e^{-t/t_R} , motivated by spring-slider models of afterslip and creep of a linear vis-
143 coelastic material respectively [*Perfettini and Avouac, 2004*]. t_R in each case refers to a relaxation
144 time of the corresponding physical process. Poroelastic deformation can also contribute to post-
145 seismic deformation [*Peltzer et al., 1998; Jónsson et al., 2003*], however we ignore this process as we
146 are limited to a two-dimensional anti-plane geometry where no volumetric strains occur.

147 Deformation due to fault afterslip is expected to be dominant at observation sites close to
148 the fault, and can be reasonably explained by a logarithmically decelerating function with relax-
149 ation times varying from days to months [*Marone et al., 1991; Hsu et al., 2006; Ingleby and Wright,*
150 *2017*]. Distributed deformation of the viscoelastic medium appears as a more diffuse and long-
151 wavelength signal in the data. The temporal evolution of this signal is not well explained by the
152 exponentially decaying solution expected from a spring-dashpot analysis; the early relaxation is
153 rapid, occurring over months, and is then followed by a much slower relaxation process [*Freed*
154 *and Bürgmann, 2004; Freed et al., 2010; Bürgmann and Dresen, 2008*]. Studies that attempt to fit the
155 observations from the first year or so of postseismic relaxation following $M_w \sim 7$ earthquakes find

156 relaxation times on the order of 1 year, whereas estimates from later time periods show relax-
 157 ation times of 10 years or more. An additional key observation from the postseismic period is
 158 that afterslip is typically observed or inferred for earthquakes down to $M \sim 3$ [Ingleby and Wright,
 159 2017; Alwahedi and Hawthorne, 2019; Hawthorne et al., 2016; Chen and Lapusta, 2009], but it has been
 160 exceedingly challenging to observe a notable viscoelastic signal following earthquake ruptures of
 161 $M_w < 7$.

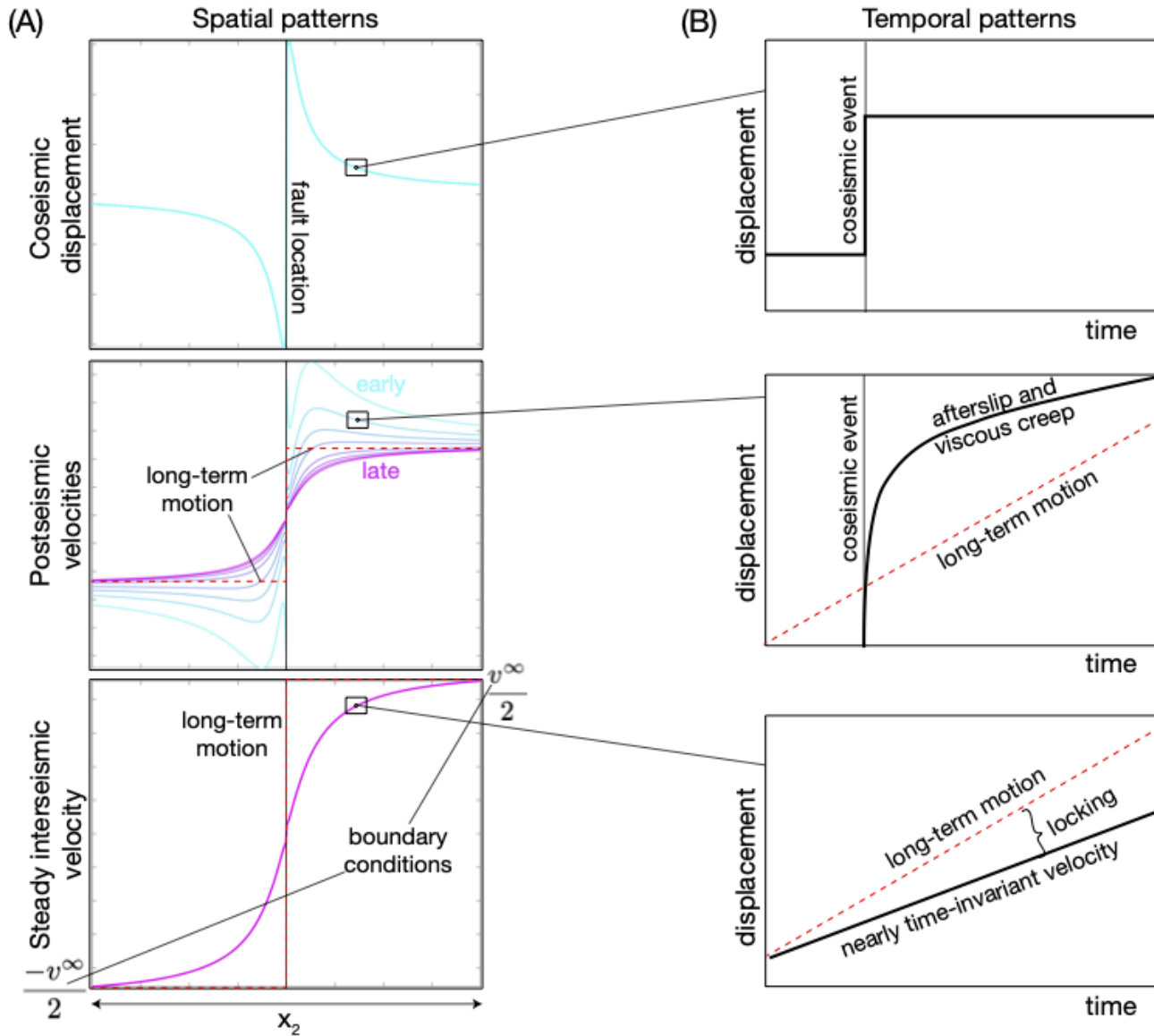


Figure 1: Schematic displacement and velocity evolution recorded at the Earth's surface over the entire earthquake cycle. We show both, (A) the spatial pattern (in colours varying from blue - early postseismic, to pink - late postseismic) and (B) the temporal evolution at a chosen location (black lines). The geodetic predictions from steady rigid block motion is shown in red dashed lines, and deviations from this motion arise due to effects of the earthquake cycle.

162 **1.3 The underlying physical and computational problem**

163 The goal is to infer the rheology of the fault and surrounding medium from the spatio-temporal
164 pattern of surface deformation that contain the features described in the previous section. Two
165 predominant modeling strategies are used for such studies - kinematic modeling of the deformation
166 field and parameter estimation using dynamic models.

167 **1.3.1 Kinematic models**

168 Kinematic models use principles of linear elasticity to develop an impulse-response type relationship
169 between unit inelastic shear and displacements at the Earth's surface [e.g., *Segall, 2010*]. This
170 set of linear relationships is then used to construct a set of normal equations to estimate slip or
171 strain distributions within the discretized domain to explain the data. The results of such an exercise
172 are estimates of the inelastic source deformation (fault slip - $\Delta s(t)$ and distributed strain -
173 $\Delta \epsilon(t)$), which then may be combined with elastic stress computations to estimate the constitutive
174 relationship between stress change and incremental slip/strain and other derivative quantities.

175 **1.3.2 Dynamic models**

176 Dynamic models take an alternative forward modelling approach, whereby equations of motion
177 are used to solve for the time-dependent bulk and surface deformation arising from an underlying
178 source process, which itself may be explicitly modeled to be time-dependent. These dynamic
179 models typically perform physics-based simulations to solve for the stress (σ) and strain-rate
180 evolution ($\dot{\epsilon}$) consistent with quasistatic equilibrium: $\nabla \cdot \sigma(\dot{\epsilon}) + f_b = 0$. f_b is the equivalent body
181 force applied to the system, which could arise from gravity or imposed slip and tractions as a
182 boundary condition [e.g., *Segall, 2010*]. The constitutive relations i.e., σ as a function of $\dot{\epsilon}$, along
183 with knowledge of the initial and boundary conditions can be used to compute the evolution of
184 deformation at the observational sites on the surface of the Earth and an optimization may be
185 performed to estimate the best-fit coefficients relating σ and $\dot{\epsilon}$.

186 The boundary conditions for this system generally correspond to Dirichlet boundaries at the
187 lateral edges of the domain (either zero or fixed plate motion depending on how the data is de-
188 composed), and traction-free boundaries at the vertical edges (e.g., Figure 2A). The initial con-
189 ditions are thought to strongly control the behaviour of the system, and generally come from an
190 estimate of the pre-earthquake velocities or strain rates in the system and an imposed stress per-
191 turbation from the coseismic event. Some modeling strategies treat the pre-earthquake strain rate
192 as a free parameter that is also estimated as part of the inverse problem.

193 **1.3.3 Decomposing the time series**

194 To simplify the inverse problem, many kinematic and dynamic modeling studies decompose the
195 observed tectonic deformation time series into additive contributions arising from (1) a constant
196 in time but spatially variable velocity field and (2) residual terms that are supposed to correspond
197 to time-dependent postseismic deformation (Figure 1). This simplification helps split the spatial
198 domain of the problem into a computationally convenient framework - by neglecting the spatially
199 variable velocity field, post-earthquake relaxation studies need only model inelastic deformation
200 sources that satisfy a zero-displacement boundary condition; a condition that is satisfied trivially
201 for a finite deformation source. A point to note is that this linear decomposition of the timeseries
202 holds exactly for kinematic methods as well as dynamic models that employ a linear rheology,
203 but can be a source of error and bias if the rheology is non-linear.

204 1.3.4 Viscoelastic earthquake cycle models

205 To circumvent issues related to far-field boundary and initial conditions, as well as data decom-
206 position, numerical studies can focus on periodic earthquake cycles. These class of models have
207 been developed in an effort to predict and explain time-dependent earthquake cycle deformation
208 consistent with not only a single earthquake, but the cumulative effects of periodic earthquake
209 sequences integrated over time (across 10's or 100's of earthquakes) to reach an approximately
210 cycle invariant state.

211 Analytic and semi-analytic interseismic velocity models have been developed assuming lin-
212 ear viscoelastic rheologies in both the cases of a finite thickness faulted elastic layer over an un-
213 bounded viscoelastic region [*Savage and Prescott, 1978; Cohen and Kramer, 1984; Hetland and Hager,*
214 *2005, 2006*], depth-averaged rheology models [*Lehner and Li, 1982; Li and Rice, 1987; Spence and Tur-*
215 *cotte, 1979*], as well as a thin viscoelastic channel [*Cohen and Kramer, 1984*]. These models use lin-
216 ear Maxwell or Burger's rheologies [*Hetland and Hager, 2005*] to describe the viscoelastic medium
217 and assume that earthquakes rupture the entire elastic layer. More recent studies account for the
218 mechanical coupling between afterslip and viscoelastic deformation. Since these models involve
219 linear rheologies, the effect of velocity boundary conditions is weak, and the inverse exercise sim-
220 ply involves fitting the curvature in the data with an optimum value of the viscosity (or viscosities
221 for a Burger's body) of the system.

222 An alternative approach is to incorporate rheological parameterizations based on laboratory
223 experiments when solving for equilibrium conditions. These laboratory-derived rheological mod-
224 els are typically determined from studies of single crystal or polycrystal assemblages of minerals
225 thought to be the dominant deforming phase in the crust (quartz) and mantle (olivine) [*Hirth,*
226 *2002; Hirth and Kohlstedt, 2003*]. These flow laws are then evaluated at values determined from ge-
227 ological estimates of compositional and thermal variations within the lithosphere to derive rock
228 rheologies at the kilometer scale [*Lyzenga et al., 1991; Reches et al., 1994; Takeuchi and Fialko, 2012,*
229 *2013*]. Recent numerical studies have incorporated viscoelastic deformation in simulations of
230 earthquake sequences along a strike-slip fault setting, providing a self-consistent framework that
231 can reproduce all aspects of the earthquake cycle, including spontaneous earthquake nucleation,
232 propagation and arrest [*Lambert and Barbot, 2016; Allison and Dunham, 2017, 2021*].

233 Both classes of numerical simulations pose their own challenges. Linear viscoelastic models
234 are borne out of computational simplicity and are able to fit many aspects of postseismic defor-
235 mation, however they predict late interseismic locking depths that are significantly deeper than
236 the brittle-ductile transition and are limited in their ability to match observations [e.g., *Takeuchi*
237 *and Fialko, 2012*]. Numerical simulations that make use of more sophisticated laboratory-derived
238 flow laws are more numerically challenging and computationally expensive [e.g., *Lambert and*
239 *Barbot, 2016*]. While they are able to better explain observations over the entire period between
240 earthquakes, their relatively high computational expense poses a challenge for coupling them
241 into an observational data-driven optimization problem, limiting their current utility for explor-
242 ing and identifying effective constitutive relations of the lithosphere. Thus, there is need for a
243 class of simulations that both satisfies the plate motion-derived kinematic boundary conditions
244 and enables efficient exploration of various rheological parameterizations in order to evaluate
245 what constraints may be afforded from surface deformation data on the effective rheology of the
246 lithosphere.

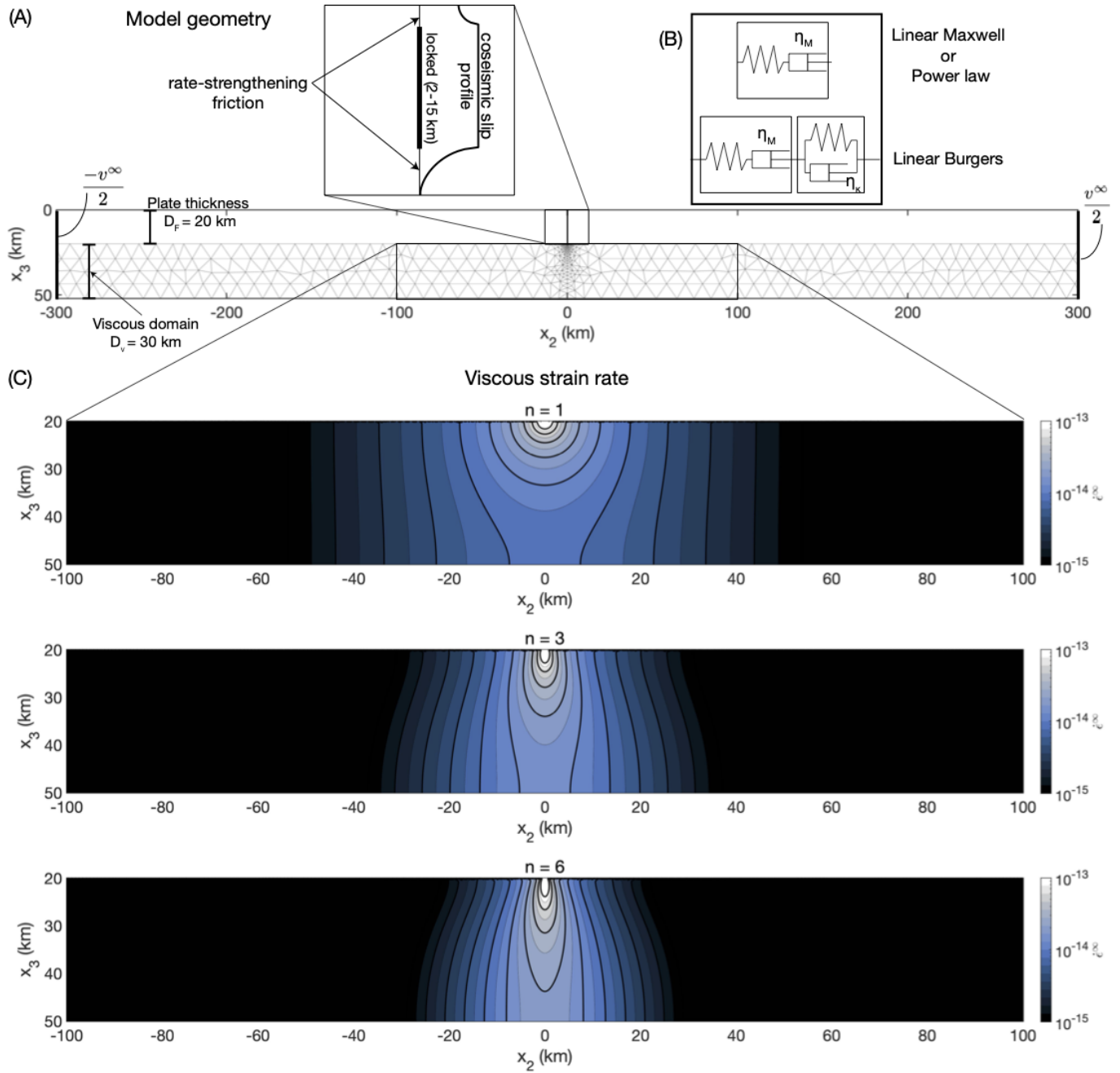


Figure 2: (A) Geometry of the numerical experiments. The domain of the stress calculations are separated into an elasto-frictional domain from 0-20 km depth and a viscoelastic domain from 20-50 km depth. Shear resistance in the frictional domain is given by rate-state friction, while the viscoelastic domain is governed by either a Maxwell rheology (the dashpot can be linear or power-law) or a linear Burgers rheology. (B) These rheologies are shown schematically. η_M - Maxwell viscosity, η_k - Kelvin viscosity. (C) Long-term viscous strain rate $\left(\sqrt{(\dot{\epsilon}_{12}^\infty)^2 + (\dot{\epsilon}_{13}^\infty)^2} \right)$ as a function of the power exponent n .

247 1.4 Aim of this study

248 In this article we discuss using earthquakes and the related cycle of loading and stress release,
249 in an idealized two-dimensional strike-slip fault geometry, to study the rheological properties of
250 the lithosphere. The aim is to develop numerical models of periodic earthquake cycles that sat-
251 isfy the applied boundary conditions in the long-term (integrated over many earthquake cycles)
252 as well as mechanical equilibrium throughout the earthquake cycle. We qualitatively compare
253 the predictions from our simulations with observations from strain-rate regimes that are orders
254 of magnitude apart, i.e., the interseismic period ($\dot{\epsilon} < \dot{\epsilon}^\infty$) and the postseismic period ($\dot{\epsilon} \geq 10\dot{\epsilon}^\infty$),
255 where $\dot{\epsilon}^\infty$ refers to the steady-state strain rate of the system or the strain rate averaged over geo-
256 logical timescales (~ 1 Ma).

257 We do not attempt to solve for a best-fit rheological description like one would in an inverse
258 problem sense. Instead, we show that linear viscoelastic rheologies need different parameters
259 to explain the interseismic and postseismic periods of the earthquake cycle, as can be modelled
260 by a Burgers rheology [e.g., *Hearn and Thatcher, 2015*], while steady state power-law rheologies
261 with power exponent $n \geq 3$ are able to simultaneously explain the observed localization of strain
262 preceding great earthquakes on mature faults, as well as the typical curvature observed in post-
263 seismic deformation timeseries.

264 2 Methods

265 Our numerical model is developed in an anti-plane geometry i.e., displacements are only in
266 the out-of-plane x_1 direction, while displacement gradients exist in the $x_2 \times x_3$ plane. We con-
267 sider a faulted elastic plate supported by a visco-elastic substrate subject to imposed boundary
268 conditions. The thickness of the elastic plate is D_F , while the viscous substrate extends from
269 $[D_F, D_F + D_V]$. The elastic plate extends infinitely in the x_2 direction, and the viscous domain is
270 chosen to be large enough to approximate this infinite x_2 extent (Figure 2A).

271 The boundary conditions for the simulations we run depend on the timescale of the problem
272 i.e., we split the problem into a viscous boundary-value problem for the long-term simulation,
273 and a set of Boundary Integral Equations to simulate the earthquake cycle [*Mallick et al., 2021*].

274 2.1 Long-term viscous strain rate

275 The governing equation for the viscous boundary-value problem is posed in terms of the scalar
276 velocity field $v(x_2, x_3)$,

$$\nabla^2 v(x_2, x_3) = - \left(\frac{\partial \log \eta}{\partial x_2} \frac{\partial v(x_2, x_3)}{\partial x_2} + \frac{\partial \log \eta}{\partial x_3} \frac{\partial v(x_2, x_3)}{\partial x_3} \right) \quad (1)$$

277 where rheology of the substrate is described as follows,

$$\frac{1}{\eta} = A \left(\sqrt{\sigma_{12}^2 + \sigma_{13}^2} \right)^{n-1} ; \quad \sigma_{1i} = \eta \dot{\epsilon}_{1i} = \eta \left(\frac{1}{2} \frac{\partial v}{\partial x_i} \right) \quad (2)$$

278 A is a rheological constant, n is the power in the power-law relation $\dot{\epsilon} = A\sigma^n$, η is the viscosity
279 and the individual stress components are σ_{1i} .

2.1.1 Boundary conditions and solution

The boundary conditions on this system are as follows: traction-free at the base ($\sigma_{13}(x_3 = D_F + D_V) = 0$); lateral edges are subject to anti-symmetric Dirichlet boundaries ($v(x_2 \rightarrow \pm\infty) = \pm \frac{v^\infty}{2}$); the entire fault slips uniformly at v^∞ resulting in rigid block-like motion of the elastic layer ($0 \leq x_3 \leq D_F$).

There exist analytical solutions to this system, as least for spatially uniform values of A, n [Moore and Parsons, 2015]. The viscous strain rates for a choice of power-law rheology only depend on n (Figure 2C) and weakly depend on the dimensions of the system. We present these solutions in terms of rescaled dimensions x'_2, x'_3 , where $x'_3 = \frac{x_3 - D_F}{D_V}$ and $x'_2 = \frac{x_2}{D_V}$. The domain for the solutions are $0 \leq x'_3 \leq 1, -\omega \leq x'_2 \leq \omega$. We choose the aspect ratio $\omega = 10$, which is sufficiently large such that there are negligible effects due to the location of the boundary on the strain-rate tensor [Moore and Parsons, 2015].

$$\begin{aligned} \frac{\dot{\epsilon}_{12}^\infty}{v^\infty} &= \frac{1}{2\omega} + \frac{1}{\omega} \left(\sum_{m=1}^{\infty} \frac{\cosh \frac{m\pi(1-x'_3)}{\omega\sqrt{n}}}{\cosh \frac{m\pi}{\omega\sqrt{n}}} \cos \frac{m\pi x'_2}{\omega\sqrt{n}} \right) \\ \frac{\dot{\epsilon}_{13}^\infty}{v^\infty} &= -\frac{1}{\omega\sqrt{n}} \left(\sum_{m=1}^{\infty} \frac{\sinh \frac{m\pi(1-x'_3)}{\omega\sqrt{n}}}{\cosh \frac{m\pi}{\omega\sqrt{n}}} \sin \frac{m\pi x'_2}{\omega\sqrt{n}} \right) \end{aligned} \quad (3)$$

We remind the reader that $\dot{\epsilon}$ refers exclusively to the viscous component of the strain rate. The total strain rate, which is a sum of the viscous and elastic components, is denoted as $\dot{\epsilon}_{\text{total}} = \dot{\epsilon} + \dot{\epsilon}_{\text{elastic}}$.

2.2 Periodic earthquake cycle simulations

The steady-state solutions for long-term viscous creep rate (Equation 3, Figure 2C) can be used to compute an equivalent background stressing rate to load earthquake cycle simulations [Mallick et al., 2021]. We note that without the long-term strain rates, one would have to assign a spatially variable long-term slip rate and strain rate to drive the earthquake cycle simulations [e.g., Lambert and Barbot, 2016], but this would not necessarily satisfy the boundary conditions of the system.

Using a background stressing rate that is kinematically and dynamically consistent with the long-term boundary conditions, we transform the time-dependent partial differential equations for quasi-static equilibrium to a set of coupled ordinary differential equations [e.g., Lambert and Barbot, 2016; Mallick et al., 2021]. Here we discuss the procedure in brief; we discretize the non-elastically deforming part of the domain using constant-slip boundary elements for faults and constant-strain boundary elements for viscous shear. These boundary elements along with Equation 3 can be used to compute the long-term loading rate of the system as follows,

$$\begin{bmatrix} \dot{\sigma}_F^\infty \\ \dot{\sigma}_{12}^\infty \\ \dot{\sigma}_{13}^\infty \end{bmatrix} = \begin{bmatrix} K_{F,F} & K_{F,12} & K_{F,13} \\ K_{12,F} & K_{12,12} & K_{12,13} \\ K_{13,F} & K_{13,12} & K_{13,13} \end{bmatrix} \begin{bmatrix} -v^\infty \\ -\dot{\epsilon}_{12}^\infty \\ -\dot{\epsilon}_{13}^\infty \end{bmatrix} \quad (4)$$

$K_{a,b}$ is a stress-interaction kernel or the boundary-element approximation of the Green's function tensor that describes the elastic stress transfer to any given element a in response to inelastic shear (slip on faults and strain in shear zones) on the considered element b [Barbot, 2018].

Deviations from the long-term loading rate (Equation 4) drive frictional slip and viscous shear within the computational domain over the earthquake cycle. The set of coupled ordinary differential equations we need to solve is therefore the instantaneous momentum balance for each

313 boundary element [e.g., *Mallick et al.*, 2021]. To do this, we account for the full elastic interaction
 314 between each point on the fault and in the viscous shear zones using the above described stress
 315 interaction kernel .

$$\begin{bmatrix} K_{F,F} & K_{F,12} & K_{F,13} \\ K_{12,F} & K_{12,12} & K_{12,13} \\ K_{13,F} & K_{13,12} & K_{13,13} \end{bmatrix} \begin{bmatrix} v - v^\infty \\ \dot{\epsilon}_{12} - \dot{\epsilon}_{12}^\infty \\ \dot{\epsilon}_{13} - \dot{\epsilon}_{13}^\infty \end{bmatrix} = \begin{bmatrix} \frac{d\sigma_{\text{friction}}}{dt} \\ \dot{\epsilon}_{12} \frac{d\eta}{dt} + \eta \frac{d\dot{\epsilon}_{12}}{dt} \\ \dot{\epsilon}_{13} \frac{d\eta}{dt} + \eta \frac{d\dot{\epsilon}_{13}}{dt} \end{bmatrix} \quad (5)$$

316 The left hand side of this set of equations is the stressing rate in the system arising from elasticity
 317 while the right hand side is the time derivative of the shear resistance provided by the rheology
 318 of the fault zone and viscoelastic medium. Details about the chosen rheologies are provided in
 319 the following section.

320 2.2.1 Friction and viscous laws

321 Resistive strength evolution on the fault (Equation 5) is described by rate-dependent friction
 322 [*Marone et al.*, 1991] i.e., the resistive strength of the fault is given by $f\sigma_n$ where f is the friction
 323 coefficient and σ_n is the effective normal strength on the fault, and reference values f_0, v_0 .

$$\sigma_{\text{friction}} = f(v)\sigma_n = \left(f_0 + (a - b) \log \frac{v}{v_0} \right) \sigma_n \quad (6)$$

324 The rheological models we test in the viscoelastic domain are the linear Maxwell, linear Burg-
 325 ers and power-law rheologies (Figure 2B). The total strain rate in these rheologies are of the form,
 326

$$\dot{\epsilon}_{\text{total}} = \frac{\dot{\sigma}}{G} + \frac{\sigma}{\eta_M} + \dot{\epsilon}_k \begin{cases} \frac{\sigma - G\epsilon_k}{\eta_k}, & \text{Burgers body} \\ 0, & \text{otherwise} \end{cases} \quad (7)$$

327 where $\dot{\epsilon}_k$ is the Kelvin strain only present for a Burgers body, η_M is the viscosity of the Maxwell
 328 element (for power-law rheologies, η_M in turn is a function of $\dot{\epsilon}$ i.e., $\frac{d\eta}{dt} \neq 0$ in Equation 5) and G
 329 is the elastic shear modulus of the system.

330 To study the role of viscous rheology in modulating the stress state in this system, and the
 331 associated displacement and velocity field at the free surface, we vary the two parameters used
 332 to describe the rheology in the viscous shear layer for the spring-dashpot bodies (linear Maxwell
 333 and power-law): A, n ; while we vary the Kelvin and Maxwell viscosities for the Burgers material:
 334 η_k, η . We also vary the recurrence time for the earthquake to see how relaxation in the lithosphere
 335 is related to the magnitude of coseismic stress perturbation. We list model parameters we varied
 336 for these simulations in Table 1.

337 2.2.2 Initial conditions from coseismic slip

338 The set of ordinary differential equations we need to solve is Equation 5 in terms of the variables
 339 $[v, \dot{\epsilon}_{12}, \dot{\epsilon}_{13}]$, subject to the rheologies in Equation 6-7. To guarantee a unique solution for this system,
 340 we need to determine the initial condition for $[v, \dot{\epsilon}_{12}, \dot{\epsilon}_{13}]$. This is done by using the stress change
 341 due to prescribed coseismic slip on the fault to instantaneously change values of $[v, \dot{\epsilon}_{12}, \dot{\epsilon}_{13}]$ subject
 342 to their rheological properties [*Montési*, 2004]. We prescribe coseismic slip as a uniform value of
 343 $u^\infty = v^\infty T_{eq}$ within the locked domain (2-15 km), and tapered in the surrounding section of fault
 344 such that the stress increase does not exceed 3 MPa and slip within this domain is minimized

Table 1: Model parameters for earthquake cycle simulations

Parameter	Range
Fault width	20 km
x_3 scale	30 km
x_2 scale	200 - 500 km
Shear modulus (G)	30 GPa
T_{eq}	50, 100, 200 yrs
ν^∞	10^{-9} m/s
Viscous layer (linear Maxwell, power-law)	
Δx	variable mesh size
n	1, 2, 3, 4, 5, 6
A^{-1}	$10^{18}, 3 \times 10^{18}, 7 \times 10^{18}, 10^{19}, 5 \times 10^{19}, 10^{20}$
Viscous layer (linear Burgers)	
Δx	variable mesh size
η_M (Pa-s)	$10^{18}, 5 \times 10^{18}, 10^{19}, 5 \times 10^{19}, 10^{20}$
η_k (Pa-s)	$5 \times 10^{17}, 10^{18}, 5 \times 10^{18}$
Fault parameters	
Δx_3	500 m
$a - b$	0.015
σ_n	40 MPa
f_0, ν_0	$0.6, 10^{-6}$ m/s

345 (Figure 2A). This is a linear inequality constrained optimization that is done using the MATLAB
 346 function *lsqlin*.

347 With the initial conditions determined from coseismic slip, we integrate the system of equa-
 348 tions using MATLAB's Runge-Kutta fourth order solver *ode45* to obtain the time history of $[v, \dot{\epsilon}_{12}, \dot{\epsilon}_{13}]$
 349 over the entire domain. Since the coseismic slip derived initial conditions only provide a change
 350 in the integrable variables, we need to run these earthquake cycles a number of times until we ob-
 351 tain cycle invariant results [e.g., *Hetland and Hager, 2005; Takeuchi and Fialko, 2012*]. In that case, the
 352 coseismic slip derived stress change is imposed every T_{eq} years. We find that, depending on rhe-
 353 ology, 10-20 cycles is sufficient to obtain cycle invariant results given the rheological parameters
 354 and timescales we have chosen.

355 2.3 Parameters that can be estimated geodetically

356 We consider two main parameters that can be inferred geodetically that are generally used to de-
 357 scribe the period following and leading up to large plate boundary earthquakes. In the postseis-
 358 mic period we estimate the effective relaxation time of the system, t_R ; we describe the interseismic
 359 signal using an effective locking depth, D_{lock} .

360 For postseismic relaxation, we consider only the deviation from steady state behaviour i.e.,
 361 we remove displacements associated with the long-term motion of the plate boundary or the
 362 steady-state strain rates ($\dot{\epsilon}_{12}^\infty, \dot{\epsilon}_{13}^\infty$). We characterize the transient surface displacements during the
 363 first 2 years following the earthquake using a two step procedure. First we use singular-value
 364 decomposition on the displacement timeseries and extract the temporal component associated

365 with the most dominant singular value. We fit this with the following functional form,

$$u(t) = \beta (1 - \exp(-t/t_R)) \quad (8)$$

366 The estimated value of t_R gives the best-fit relaxation time of the system over the observational
367 window [Perfettini and Avouac, 2004].

368 Later in the earthquake cycle, we consider the interseismic period as the time period when the
369 maximum surface velocity is smaller than the relative plate velocity i.e., $|v(x_2)| \leq \frac{v^\infty}{2}$. The resulting
370 velocity field can then be fit to an arc-tangent function [Savage and Burford, 1973],

$$v(x_2) = \frac{v^\infty}{\pi} \tan^{-1} \left(\frac{x_2}{D_{lock}} \right) \quad (9)$$

371 The estimated locking depth controls the effective width of the surface that is experiencing inter-
372 seismic strain, and is thus a physically motivated representation of the spatial pattern of the
373 signal.

374 3 Results

375 We describe the surface deformation observations predicted at geodetic sites over the entire earth-
376 quake cycle, as well as the corresponding strain rate evolution within the viscoelastic domain from
377 our numerical experiments (Figure 3, 4). Since we are interested in cycle invariant behaviour, we
378 only present results from the last earthquake cycle; the previous cycles are necessary only for spin
379 up. The results are discussed separately for linear Maxwell, linear Burgers and power-law rhe-
380 ologies in terms of interseismic locking depths (Figure 5), cumulative postseismic displacements
381 (Figure 6) and effective relaxation timescales (Figure 7).

382 3.1 Linear Maxwell

383 For linear Maxwell rheologies, both the amplitude and effective relaxation timescale of the post-
384 seismic response directly depend on the viscosity (η_M). As η_M increases, the timescale for stress
385 relaxation following the coseismic perturbation (t_R) increases, while the magnitude of the initial
386 jump in strain rate ($\Delta\dot{\epsilon}(\Delta t = 0)$) decreases.

$$t_R = \frac{\eta_M}{G} \quad (10)$$

$$\Delta\dot{\epsilon}_M(\Delta t = 0) = \frac{\Delta\tau_{co}}{\eta_M} \approx \frac{K(v^\infty T_{eq})}{\eta_M}$$

387 A dominant feature from simulations incorporating a linear Maxwell rheology is that they
388 show strain rates that are diffusive in space and in time (Figure 3A). The initial strain rate following
389 the earthquake decays in space as expected from the stress change $\Delta\tau_{co}$. In time, the elevated strain
390 rate is damped as it diffuses outwards. At the end of the earthquake cycle ($\Delta t/T_{eq} \rightarrow 1$), nearly the
391 entire viscoelastic medium is at a uniform strain rate level and the resulting surface velocity field
392 appears to have a near constant spatial gradient (Figure 4D).

393 Many aspects of the evolution of this viscoelastic system can be explained by a single dimen-
394 sionless variable, $\tau_M = \frac{T_{eq}}{2t_R} = \frac{GT_{eq}}{2\eta_M}$ [Savage and Prescott, 1978; Savage, 2000]. Models with $\tau_M \gg 1$
395 generate relatively large magnitude postseismic deformation early in the earthquake cycle and
396 predict relatively small near fault velocity gradients late in the earthquake cycle. Conversely, if

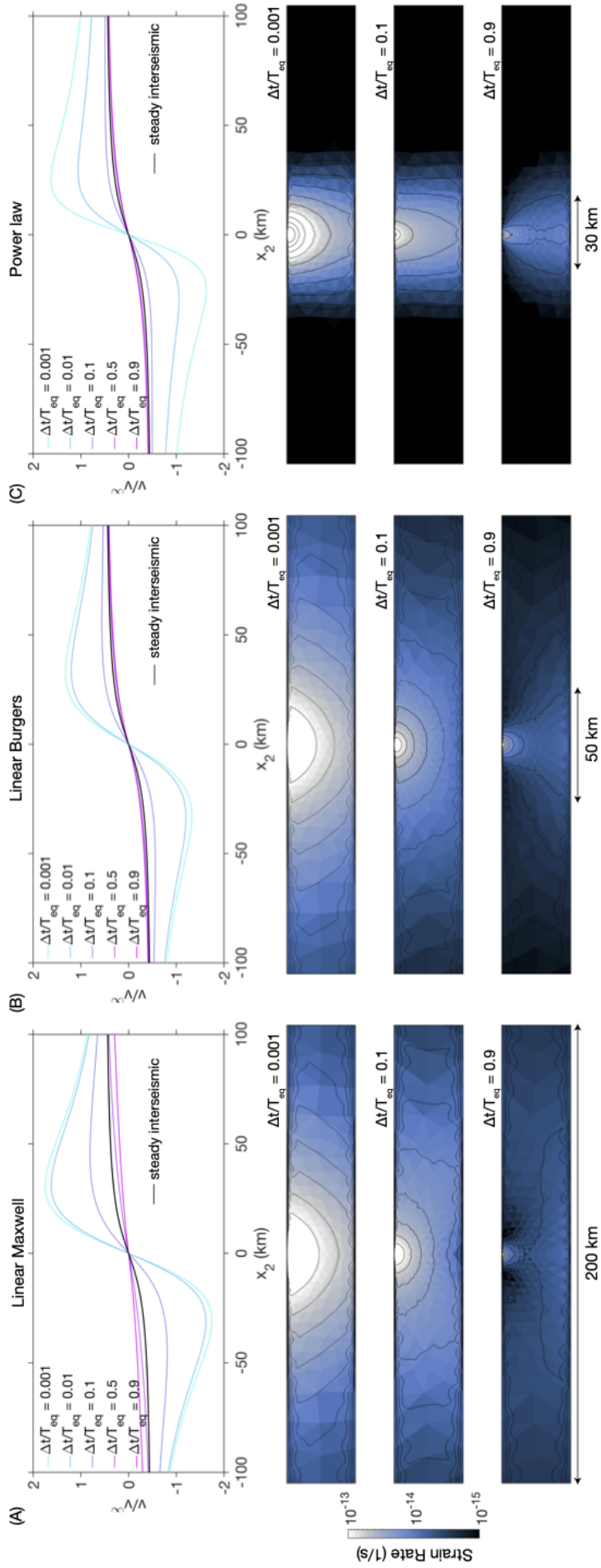


Figure 3: Surface velocity and internal viscous strain rate evolution over the earthquake cycle for different rheologies for a periodic earthquake cycle of $T_{eq} = 50$ years. The rheologies were chosen such that the early postseismic surface velocity field is nearly identical. (A) Linear Maxwell body ($\eta_M = 3 \times 10^{18}$ Pa-s), (B) Linear Burgers body ($\eta_k = 3 \times 10^{18}$ Pa-s, $\eta_M = 5 \times 10^{19}$ Pa-s) and (C) Power law rheology ($A^{-1} = 3 \times 10^{18}$, $n = 3$). The linear rheologies allow accelerated viscous deformation of significantly larger volume of material compared to the power-law rheology, which promotes localization of strain. This effect is noticeable in all the strain rate snapshots.

397 $\tau_M \ll 1$, the model behavior approaches the elastic limit where there is negligible viscous re-
 398 sponse and the predicted surface velocities vary only moderately around the steady state elastic
 399 expectation throughout the earthquake cycle.

400 3.1.1 Interseismic locking depth

401 Systems characterized by large τ_M , which could arise from large T_{eq} or small t_R , result in large
 402 locking depths at the end of the interseismic period while low τ_M systems show significantly
 403 smaller locking depths (Figure 5A-B). An additional feature is that the estimated locking depth
 404 in these simulations increases monotonically in time, with the amplitude of this time-dependence
 405 directly related to τ_M (Figure 5D).

406 3.1.2 Postseismic creep and relaxation time

407 Postseismic velocities following an earthquake decay exponentially for linear Maxwell bodies
 408 beyond a short, initial acceleration period. This acceleration period scales with the logarithm of
 409 η_M . The time constant for the subsequent decay is the relaxation time of the system (t_R), and it is
 410 a material property (Figure 6). As a result, T_{eq} does not affect the estimated t_R value or the spatial
 411 pattern of postseismic deformation (Figure 6,7).

412 3.2 Linear Burgers

413 The linear Burgers rheology is characterized by two separate timescales: a short-term anelastic
 414 timescale $\frac{\eta_k}{G}$ controlled by the viscosity of the Kelvin element, and a long-term Maxwell timescale
 415 $\frac{\eta_M}{G}$ (assuming $\eta_k < \eta_M$) [Müller, 1986; Hetland and Hager, 2005]. Only the creep associated with
 416 the Maxwell element is recorded as permanent strain, the anelastic term is significant for geodetic
 417 observations but does not leave a record in the long-term.

418 Similar to the linear Maxwell case, the linear Burgers body also exhibits a tendency to diffuse
 419 strain rate away from the fault with time (Figure 3C). This pattern depends on three variables - T_{eq} ,
 420 and the two relaxation times associated with η_k and η_M . Large values of η_k, η_M resemble an elastic
 421 medium, and small values of T_{eq} lead to small stress perturbations and hence minimal deviation
 422 from a time-invariant steady-state model. Small values of η_k and η_M , or large values of T_{eq} lead
 423 to more pronounced earthquake cycle effects. The effects of these quantities can be understood
 424 by examining the instantaneous strain rate change in the Kelvin and Maxwell elements due to
 425 coseismic slip.

$$\begin{aligned} \Delta \dot{\epsilon}_k(\Delta t = 0) &\approx \frac{K(v^\infty T_{eq})}{\eta_k} \\ \Delta \dot{\epsilon}_M(\Delta t = 0) &\approx \frac{K(v^\infty T_{eq})}{\eta_M} \end{aligned} \quad (11)$$

426 The subsequent relaxation follows an initial relaxation controlled by η_k which then smoothly tran-
 427 sitions to the relaxation timescale of η_M . The transition timescale is controlled by the ratio of $\frac{\eta_k}{\eta_M}$
 428 [Hetland and Hager, 2005]. While we do not consider scenarios of $\frac{\eta_k}{\eta_M} > 1$ in our simulations, the
 429 reduction of a Burgers system to a Maxwell body is possible by increasing $\frac{\eta_k}{\eta_M} \rightarrow \infty$ since at that
 430 limit there is no transient strain in the Kelvin element anymore.

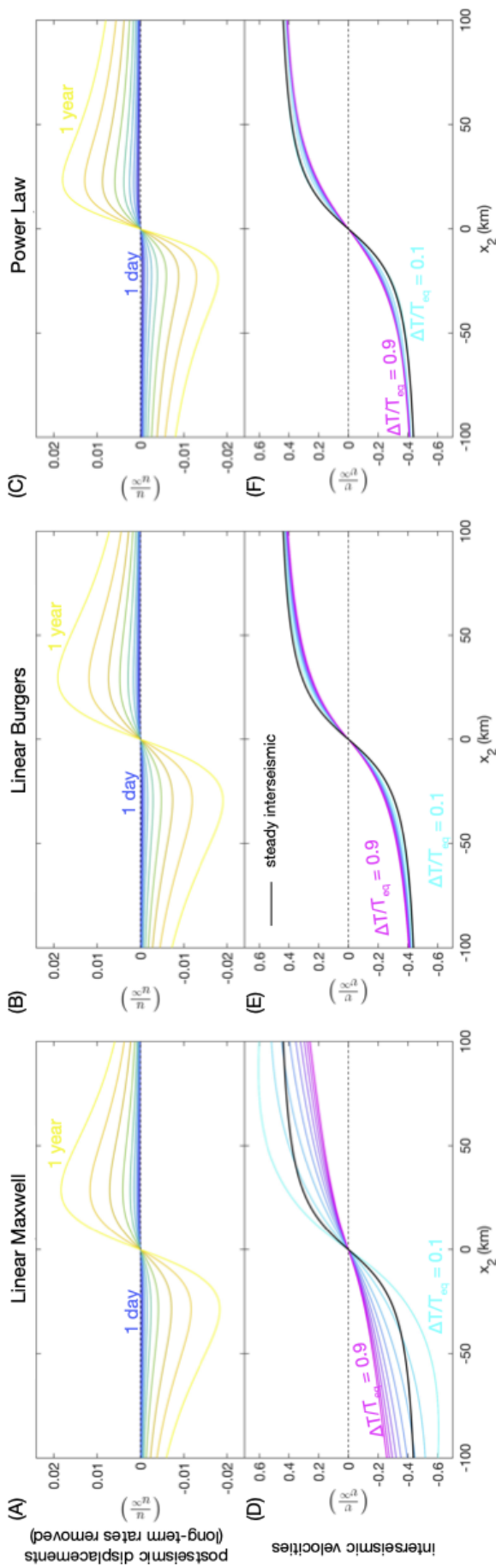


Figure 4: Surface predictions of postseismic displacements and interseismic velocities for different rheologies for a periodic earthquake cycle of $T_{eq} = 100$ years. The rheologies are chosen such that the cumulative postseismic after 1 year is nearly identical for all three models. (A)-(C) Cumulative postseismic displacements normalized by the coseismic slip amount ($u^\infty = v^\infty T_{eq}$) for times varying from 1 day to 1 year. (D)-(F) Interseismic velocities compared to the steady interseismic expectation (black line).

431 3.2.1 Interseismic locking depth

432 Late interseismic locking depths show systematic dependence on only two parameters - η_M and
433 T_{eq} (Figure 5C). η_k controls the early postseismic response but does not contribute to the late
434 interseismic behaviour. Larger η_M produces smaller locking depths while increasing T_{eq} increases
435 the locking depths, which suggests that late interseismic behaviour of this system is controlled
436 by the same dimensionless parameter as the linear Maxwell case, $\tau_M = \frac{GT_{eq}}{2\eta_M}$ [Savage and Prescott,
437 1978; Savage, 2000]. The estimated locking depth for simulations with small effective τ_M , due to
438 low T_{eq} or large η_M , are comparable to a purely frictional-elastic simulation and show a nearly
439 time-invariant behaviour (Figure 5D).

440 3.2.2 Postseismic creep and relaxation time

441 Linear Burgers bodies do not have a single relaxation timescale, and thus our estimates of t_R
442 depend on the time window that is considered. However, this relaxation timescale is independent
443 of the coseismic slip magnitude and thus has no dependence on T_{eq} . We consider a 2-year time
444 window, which is a typical observational window used in geodetic studies, in order to estimate
445 the relaxation time and effective viscosity of the system. In most of our simulations, this estimated
446 relaxation time corresponds to sampling the viscous relaxation controlled by η_k . Higher values of
447 η_k lead to larger relaxation times, with the effect of η_M being negligible for the 2-year observational
448 window and the parameter range we considered (see caption in Figure 6).

449 3.3 Power-law

450 Our numerical experiments governed by power-law rheologies are characterized by two main fea-
451 tures - (1) the interseismic locking depths appear to be a constant in time and only weakly sensitive
452 to the parameters we varied (Figure 5A-B), and (2) the postseismic relaxation timescale and ampli-
453 tude appear to depend on the coseismic slip amplitude and conform poorly to the $\exp(-t/t_R)$
454 functional form we chose to fit it with (Figure 4C, 7B), i.e., the curvature in the timeseries is closer
455 to a logarithmic decay than the exponential function we chose [e.g., Montési, 2004].

456 3.3.1 Localized deformation and interseismic locking depth

457 For our simulations with power-law rheologies, deformation throughout the entirety of the earth-
458 quake cycle is significantly more localized in space than as observed for the linear viscoelastic
459 rheologies discussed above (Figure 3C). The extent of localization depends on the power expo-
460 nent n as well as the rheological parameter A . We contrast this with the fact that the solution to
461 the long-term viscous boundary value problem does not depend on A (Equation 3). Thus, our
462 simulation results suggest that both A and n may be inferred from geodetic data by combining
463 insight throughout the entire earthquake cycle.

464 Larger stress exponents n favor increased localization while large coefficients A reduce the
465 impact of stress perturbations from coseismic slip, similar to how the magnitude of the viscosity
466 of linear rheologies controls the change in strain rates in Equation 10. While the degree of strain
467 localization depends on the power law stress exponent, for the parameter space explored, we
468 find that models with power law exponents $n \geq 3$ exhibit nearly identical late interseismic locking
469 depths (Figure 5A,D), and are generally comparable to simple back-slip models of interseismically
470 locked faults.

471 3.3.2 Postseismic creep and relaxation time

472 The postseismic deformation timeseries is not expected to conform to the exponential functional
473 form we used to fit the timeseries. This is because the exponential function is a solution to the
474 linear viscoelastic problem [Perfettini and Avouac, 2004,], and the outputs of a power-law rheology
475 correspond to an effective viscosity that systematically increases in time [Montési, 2004]. How-
476 ever, since we consider time windows on the order of 1-2 years, the relaxation timescale can be
477 fit using a linear viscoelastic approximation to estimate an average relaxation time over that win-
478 dow. These relaxation timescales are not only dependent on rheological parameters A, n but are a
479 function of the earthquake size, parameterized here in terms of coseismic slip (Figure 6).

480 For a given set of rheological parameters A, n (for $n > 1$), the cumulative postseismic deforma-
481 tion over a given time window (in this case $\Delta t = 2$ years), even when normalized by the coseismic
482 slip amount, increases with earthquake size (Figure 7A). The normalized postseismic deformation
483 following small earthquakes in our simulations ($u^\infty \sim 1.5\text{m}$) amounts to about 30% of the normal-
484 ized postseismic deformation following the largest earthquakes ($u^\infty \sim 12\text{m}$). On the other hand,
485 the estimated relaxation timescale decreases with increasing earthquake size (Figure 7B).

486 4 Discussion

487 We have developed numerical earthquake cycle experiments in order to test how well popular
488 rheological models are able to qualitatively reproduce different observational features in geodetic
489 studies over the entire interseismic period. Our simulation results illustrate the non-uniqueness
490 of rheological models, and their parameters, in explaining postseismic data alone (Figures 5-7).
491 However, we demonstrate how this non-uniqueness can be mitigated to some extent by incorpo-
492 rating data corresponding to strain accumulation in the late interseismic period (Figure 5). We
493 find that steady-state power-law rheologies with $n \geq 3$ as well as linear Burgers rheology with
494 $\eta_M \approx 10^{20}$ Pa-s and $\eta_k \approx 10^{18}$ Pa-s are able to explain early postseismic relaxation as well as the
495 strain localization observed near strike-slip faults late in the interseismic period. While we do not
496 show it explicitly, nonlinear Burgers rheologies with $n \geq 1$ (with relevant A values) could explain
497 the geodetic data just as well. This is because a steady-state rheology, linear or power-law, is sim-
498 ply a limiting case of an appropriate Burgers rheology where the transient viscosity is much larger
499 than the steady-state value. On the other hand, linear Maxwell rheologies are simply insufficient
500 to explain the observational features.

501 In the following sections, we first discuss the equivalence between linear Burgers and power-
502 law descriptions of lithospheric rheology for the earthquake cycle, and then detail geophysical
503 observations that may be required to convincingly discriminate between these two rheologies.
504 We then expound on the relationship between inferences of average rheological parameters from
505 crustal scales and those measured in laboratory experiments, and how a power-law rheology is
506 consistent with both geodetic observations and laboratory-derived flow laws. Finally, we con-
507 clude with the implications for stress transfer and the associated assessment of regional hazard
508 when frictional and viscous creep are mechanically coupled.

509 4.1 The effective rheology of the lithosphere

510 Geodetic investigations of lithospheric rheology, specifically the lower crust and uppermost man-
511 tle, that consider only a relatively short time window ($\Delta t < 5$ years) as is typical of geodetic post-
512 seismic studies, may not be able to distinguish between any of the rheological models discussed in

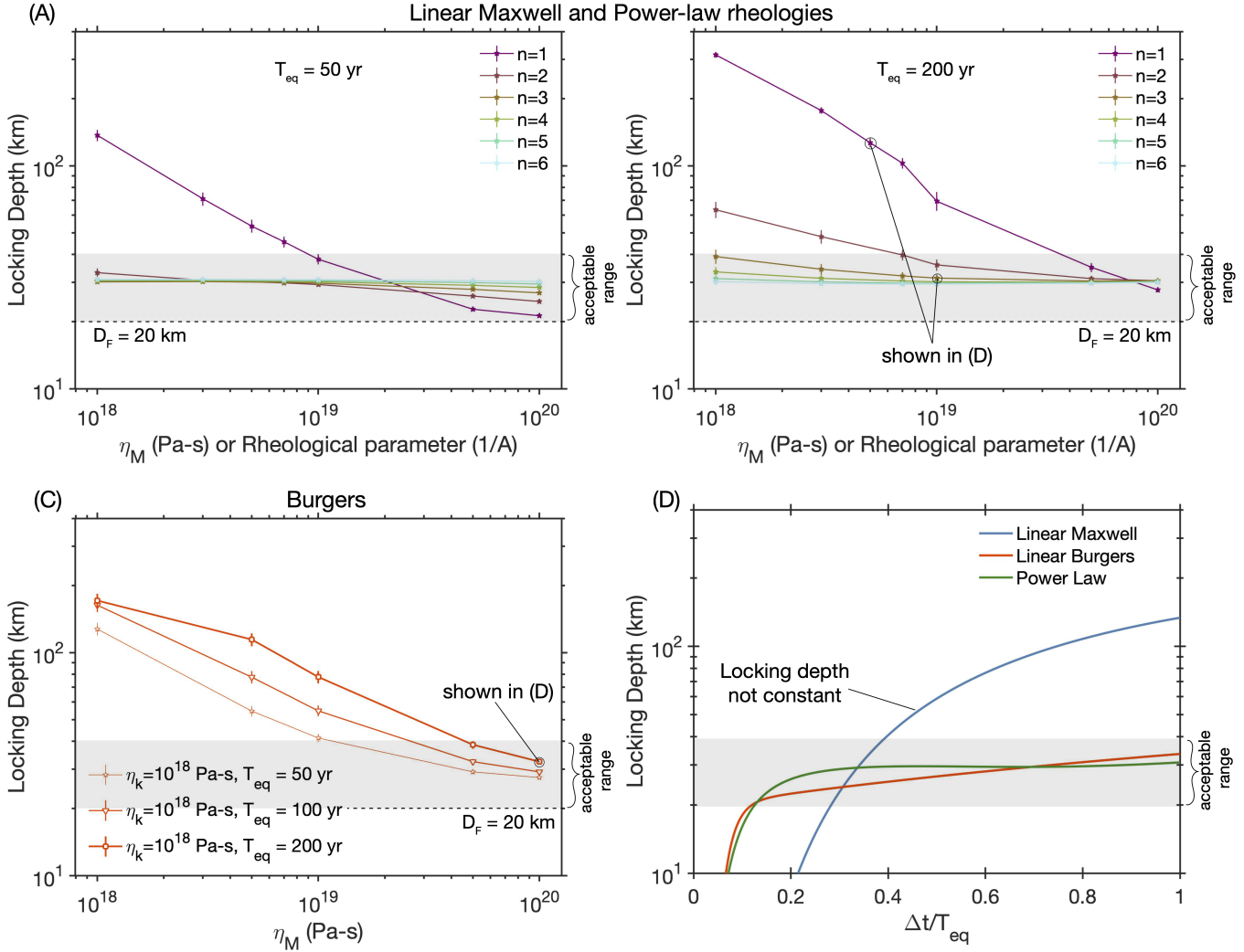


Figure 5: Compilation of late interseismic locking depths for various rheological choices and two different T_{eq} . Locking Depth (assuming an arc-tangent functional fit - $\frac{v^\infty}{\pi} \tan^{-1} \frac{x_2}{D}$) for (A) Linear Maxwell and power-law materials with n varying from 1 to 6 for $T_{eq} = 50$ years. (B) Same as (A) for $T_{eq} = 200$ years. (C) Locking depths for a linear Burgers rheology for a constant η_k and varying η_M and T_{eq} . Late interseismic locking depths show no dependence on η_k . (D) The estimated locking depth varying in time over the interseismic period for different rheologies. Both the power-law body and linear Burgers (with large η_M) show nearly time invariant late-interseismic locking depth.

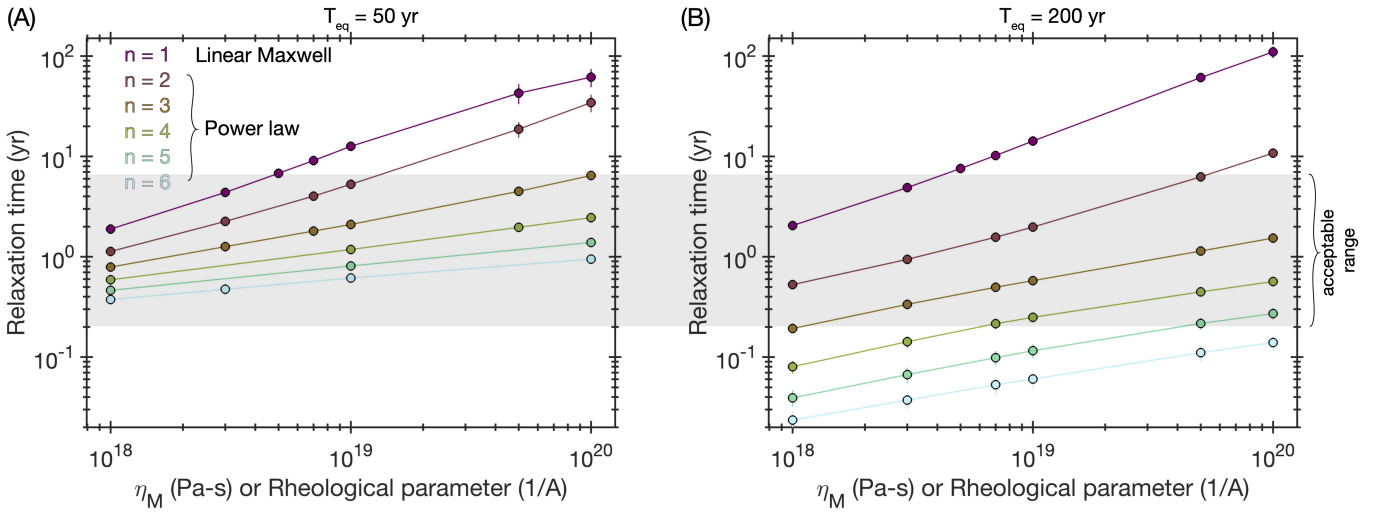


Figure 6: Postseismic relaxation times for linear Maxwell and power law bodies estimated over a 2 year period following the earthquake for a recurrence interval of (A) 50 years and (B) 200 years. Increased T_{eq} leads to larger coseismic slip ($u^\infty = v^\infty T_{eq}$), and hence larger stress change to drive postseismic creep. Linear Maxwell bodies follow a stress-independent relaxation time given by $t_R \approx \frac{\eta_M}{G}$. The relaxation time of power law bodies show a significant reduction for larger coseismic slip. We do not show the results for Burgers bodies since their relaxation times over the given time window are exactly as predicted by the viscosity of the Kelvin element $t_R \approx \frac{\eta_k}{G}$.

513 this paper (linear Maxwell, linear Burgers and power-law). This is because postseismic geodetic
 514 observations can be reduced into two features - a spatial pattern of cumulative postseismic deforma-
 515 tion and the effective relaxation timescale (Figure 7), and there exists a non-unique mapping
 516 between rheological parameters from each of the discussed rheological models to these spatial
 517 and temporal patterns of the deformation data (Figure 7 - 8A-B).

518 However, the three rheological models display diverging behavior as the observational win-
 519 dows gets larger; this is what we exploit during the late interseismic period. Interseismic strain
 520 localization and the stationarity of the locking depth in time is observed in models with either a
 521 power-law rheology or a linear Burgers rheology that approximates the effective viscosity evolu-
 522 tion of a power-law body (Figure 8D). In contrast, linear Maxwell rheologies promote diffuse
 523 strain distributions (Figure 3) which manifests as an increase in effective locking depths late in the
 524 earthquake cycle (Figure 5D), a feature that is not seen even in the best monitored strike-slip fault
 525 systems in the world [e.g., Hussain *et al.*, 2018]. This leads us to suggest that Earth's lithosphere
 526 cannot be well-described by a homogenous linear Maxwell body, at least over the timescale of the
 527 earthquake cycle.

528 These findings do not invalidate previous work on estimating the effective viscosity from post-
 529 seismic, post-glacial and lake rebound deformation observations assuming a linear Maxwell rhe-
 530 ology [e.g., Kenner and Segall, 2003; Johnson and Segall, 2004; Devries and Meade, 2013; Tamisiea *et al.*,
 531 2007; England *et al.*, 2013; Kaufmann and Amelung, 2000; Larsen *et al.*, 2005]. However, the important
 532 implication is that these estimates of the average viscosity, or viscosity structure, are tied to the
 533 observational window. This detail becomes apparent when comparing the lithospheric viscosi-
 534 ties estimated from processes that occur over different timescales; longer observations windows
 535 typically show significantly higher viscosities e.g., the viscosity of the upper mantle estimated fol-
 536 lowing deglaciation (since the Last Glacial Maximum), which represents a 10^4 year observational
 537 time window, is between $10^{20} - 10^{21}$ Pa-s [e.g., Tamisiea *et al.*, 2007; Milne *et al.*, 2001] while typical

538 viscosities estimated in the decade(s) following $M_w > 7$ earthquakes range from $10^{18} - 10^{19}$ Pa-s
 539 [e.g., *Kenner and Segall, 2003; Pollitz, 2005; Ryder et al., 2007*]. Both power-law and linear Burgers
 540 rheologies can help reconcile these apparently disparate viscosity estimates since both processes
 541 produce time-dependent viscosities which increase with time since the applied stress perturbation
 (Figure 8D).

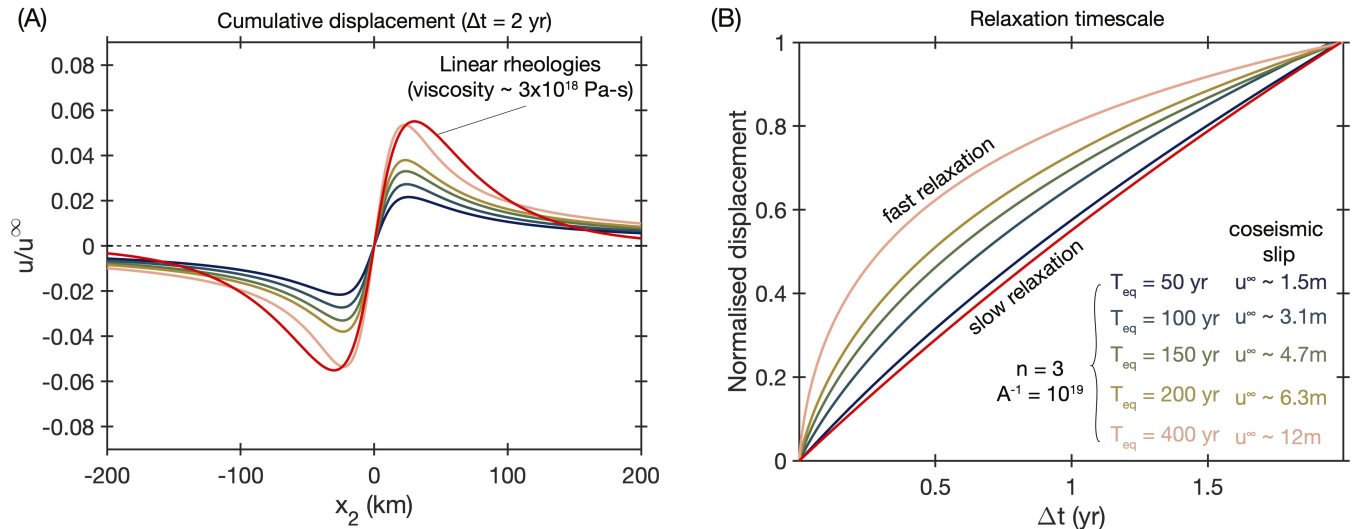


Figure 7: Magnitude dependent postseismic motions for power law bodies. (A) Cumulative postseismic displacement (steady state component removed) normalized by the coseismic slip amount ($u^\infty = v^\infty T_{eq}$) over 2 years for the same rheology. By increasing the earthquake recurrence interval, we increase the coseismic slip amount. Only power law materials show increasing cumulative deformation with increase in the recurrence interval. (B) As the cumulative deformation increases, the relaxation timescale decreases i.e., the postseismic deformation becomes faster and larger.

542

543 4.1.1 Similarities between power-law and linear Burgers rheologies

544 A question that arises at this point is - how can a linear and power-law rheology satisfactorily
 545 explain deformational data throughout the earthquake cycle? The near equivalence between linear
 546 Burgers and power-law bodies in our simulations exists because of a non-unique mapping
 547 between rheological parameters for each model and the observational features that we use to
 548 describe the deformation timeseries (Figure 8A-C).

549 Consider the viscosity evolution of a power-law body. The power-law rheology results in a
 550 lower effective viscosity during the relatively high stress and strain rate postseismic period, and
 551 the viscosity gradually increases as stress relaxes and decays to a near time-invariant interseismic
 552 state (Figure 8D). The linear Burgers rheology captures this same kinematic behaviour through
 553 completely different dynamics. The Burgers description can be thought of as a technique to de-
 554 scribe non-steady state viscous rheology i.e., there exists a finite timescale or strain over which the
 555 system has to evolve to reach the unique mapping between stress and strain rate [*Müller, 1986;*
 556 *Hetland and Hager, 2005*]. In the case of a linear Burgers rheology, the initial low effective viscosity
 557 during the postseismic period is a disequilibrium feature that smoothly evolves to its significantly
 558 larger steady state viscosity (Figure 8D).

559 While the overall kinematics predicted by the two different rheological models appear similar,
 560 the predictions from the two models are not identical (Figure 8A inset). Although they would

561 likely be difficult to distinguish after considering the errors and uncertainties in typical geodetic
562 datasets and the various models employed to fit the data [Duputel et al., 2014; Minson et al., 2013].

563 4.1.2 Magnitude-dependent postseismic motions

564 Our simulation results suggest that linear Burgers and power-law rheologies may in principle be
565 distinguished by the sensitivity and rate of the postseismic moment release to the magnitude of
566 the coseismic event. For a typical time window ($\Delta t = 2$ yrs), linear viscoelastic rheologies result
567 in postseismic surface deformation that is a linear function of the coseismic slip ($u^\infty = v^\infty T_{\text{eq}}$), and
568 thus can be normalized to produce a constant shape (Figure 7A). Similarly, the temporal evolution
569 of this moment release is invariant of the size of the earthquake (Figure 7B). In contrast, power-law
570 rheologies show a clear magnitude dependence, where the normalized postseismic deformation
571 at the surface is smaller for small events and grows larger with increasing coseismic slip (Figure
572 7A). The temporal evolution of moment release is also a function of event size with smaller events
573 having much slower relaxation than larger events (Figure 7B).

574 While this magnitude-dependent behaviour has not been studied thoroughly, there is some
575 evidence to suggest the existence a magnitude-dependent pattern in postseismic observations,
576 supporting the interpretation that lithospheric deformation may follow a power-law rheology.
577 For example, multi-year post-seismic viscoelastic deformation has been clearly observed and docu-
578 mented following $M_w > 7$ continental earthquakes [e.g., Savage and Swarc, 2009; Wen et al., 2012;
579 Wang and Fialko, 2018; Freed and Bürgmann, 2004; Freed et al., 2010; Zhao et al., 2021; Pollitz, 2019;
580 Moore et al., 2017; Tang et al., 2019], however observations of notable viscoelastic deformation fol-
581 lowing slightly smaller ($6.5 < M_w < 7.0$) continental earthquakes are equivocal [e.g. Savage et al.,
582 1998; Wimpenny et al., 2017; Bruhat et al., 2011]. Such distinction in observed postseismic behav-
583 ior for different sized earthquake ruptures may indicate a critical coseismic stress perturbation
584 required to activate geodetically detectable viscous flow, as would be expected from power-law
585 rheologies (Figure 7). Identifying a clear magnitude-dependence of postseismic viscous response
586 may be challenging given the limited historical data available for individual fault segments, how-
587 ever a careful global compilation of postseismic deformation over a fixed time window following
588 strike-slip fault earthquakes ranging from M_w 6-8 may provide further insight to any systematic
589 magnitude-dependent response, and help discriminate between rheological models of the litho-
590 sphere.

591 4.2 What do estimates of A and n mean at the lithospheric scale?

592 As previously discussed, geodetic data over a single earthquake cycle is consistent with two
593 classes of rheological models: (1) steady-state flow laws with power law exponents $n \geq 3$ and
594 a range of A values, and (2) an unsteady flow law with $n = 1$, $\eta_k/\eta_M < 0.1$, and $\eta_M \geq 10^{20}$ Pa-s. We
595 note that for unsteady flow laws, we have only explicitly considered the linear Burgers rheology
596 ($n = 1$); a power-law rheology with an additional unsteady or transient element can exactly re-
597 produce the observations as well. The principle of parsimony would suggest that a steady-state
598 power-law rheology presents a better representation of the lithosphere, but we turn to the liter-
599 ature from the mineral physics community to expound on the appropriate rheological choice as
600 well as how to interpret what are essentially kilometre-scale averaged estimates of rheological
601 parameters \hat{A} , \hat{n} (and $\hat{\eta}_k$) from geodetic data.

602 There are two main aspects to this discussion - (1) the contribution of multiple different mech-
603 anisms to the inferred parameters (\hat{A} , \hat{n} , $\hat{\eta}_k$), (2) the spatially heterogeneous variations of the pa-
604 rameters of various mechanisms to our spatially uniform estimates of the inferred rheological

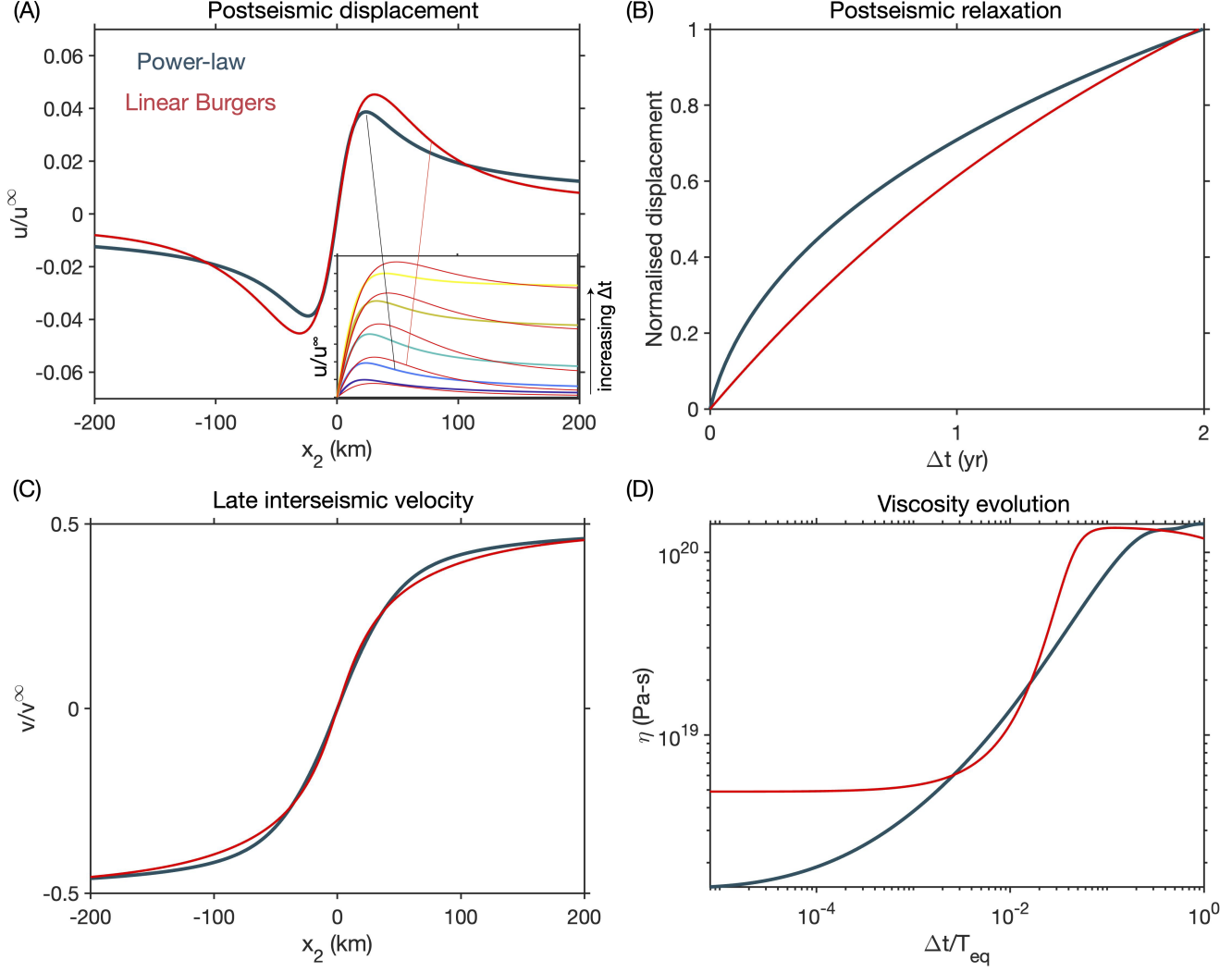


Figure 8: Approximating power-law rheology ($A = 10^{19}$, $n = 3$) with a linear Burgers body ($\eta_M = 10^{20}$ Pa-s, $\eta_k = 3 \times 10^{18}$ Pa-s) for $T_{eq} = 200$ years. (A) Cumulative displacement for power-law and linear Burgers rheologies after 2 years. The inset shows snapshots of cumulative deformation over increasing time windows of 0.5, 2, 10, 30, 50 years (blue - short timescale, yellow - long timescale). (B) Relaxation time function extracted from the timeseries. (C) Late interseismic velocity field. (D) Average viscosity evolution in time for both rheological models. $\eta(\Delta t) = \frac{\iint \eta(x_2, x_3, \Delta t) |\dot{\epsilon}(x_2, x_3, \Delta t)| dx_2 dx_3}{\iint |\dot{\epsilon}(x_2, x_3, \Delta t)| dx_2 dx_3}$

where $|\dot{\epsilon}| = \sqrt{\dot{\epsilon}_{12}^2 + \dot{\epsilon}_{13}^2}$

605 parameters.

606 4.2.1 Averaging over multiple mechanisms and assemblages

607 The simplified rheology we employ in this article (Equation 2) is a composite flow law, that under
608 the assumption of linear mixing would attempt to approximate a linear combination of multiple
609 micro-scale processes in the following way,

$$\dot{\epsilon} = \hat{A}\sigma^{\hat{n}} \approx \sum_i \left[c_i \exp\left(-\frac{Q_i + PV_i^*}{RT}\right) d^{-m_i} C_{\text{fluid}}^{r_i} \right] \sigma^{n_i} \quad (12)$$

610 This summation indicates simultaneously active processes with different values of the power-
611 law exponent (n_i), each having material specific corresponding activation energy and volumes
612 (Q_i, V_i^*), grain size dependence (m_i) and fluid phase dependence (r_i). c_i is a material and process
613 specific constant, C_{fluid} may refer to either the water fugacity or melt fraction, R is the universal
614 gas constant, T is the absolute temperature of the system and d is a central tendency of the grain
615 size distribution in the sample.

616 Power-law rheologies for rocks with stress exponents of $n \sim 3 - 4$ are considered representa-
617 tive of dislocation creep, where deformation is accommodated by the migration of dislocations
618 and dislocation planes within the crystal lattice [e.g., *Chopra and Paterson, 1981; Hirth and Kohlstedt,*
619 *2003*]; linear rheologies indicate the diffusion of vacancies and defects through the mineral
620 grains and grain boundaries [e.g., *Rutter and Brodie, 2004; Karato et al., 1986*]; intermediate values
621 of n have been suggested to be related to grain boundary sliding [e.g., *Hansen et al., 2011; Goldsby*
622 *and Kohlstedt, 2001*], although it is important to note that this mechanism is intrinsically coupled
623 to either diffusion or dislocation creep [*Raj and Ashby, 1971; Hansen et al., 2011*]. In addition to
624 mechanical processes, thermal effects can also be relevant to lithospheric deformation. Thermal
625 effects are typically thought of in terms of the steady-state geothermal gradient, but this thermal
626 profile can be perturbed by viscous heating during rapid shear and an associated thermal diffu-
627 sion [*Takeuchi and Fialko, 2013; Moore and Parsons, 2015*]. As a consequence, the effective power law
628 \hat{n} inferred at the kilometer scale need not be bounded between 1 and 4, but instead may be even
629 higher [e.g., *Kelemen and Hirth, 2007*].

630 If any of the individual parameters in Equation 12 evolve with incremental strain or time e.g.,
631 temperature or grain size [*Allison and Dunham, 2021; Montési and Hirth, 2003*], then there would not
632 be a unique relationship between $\dot{\epsilon}$ and σ until a steady state is reached. The viscous creep that
633 would result from this equilibration process is often called ‘transient creep’, and is an important
634 motivation for invoking Burgers rheology [*Post, 1977; Chopra, 1997; Freed et al., 2012*]. Despite
635 the likely presence of viscous transients, we maintain that the principle of parsimony dictates
636 that we choose steady-state power-law rheologies over Burgers rheologies for modeling geodetic
637 data. To further illustrate this preference, we draw parallels between the aforementioned transient
638 viscous creep and deviations from steady-state frictional strength in rock friction experiments.
639 Unsteady evolution of the friction coefficient is captured by a state variable, θ , which is thought
640 to represent the quality and/or average timescale of asperity contact during frictional sliding
641 [*Marone, 1998; Scholz, 1998*]. Despite the well-known importance of θ to many aspects of frictional
642 mechanics [*Scholz, 2002*], geodetic investigations of frictional afterslip are rarely able to resolve
643 the evolution of the frictional state from the data. Even when the state evolution is identified,
644 it is shown to quickly evolve towards steady state within a few hours and may be invisible to
645 typical (sampled daily) postseismic timeseries [*Fukuda et al., 2009; Perfettini and Ampuero, 2008*].
646 This argument does not obviate the existence or importance of unsteady strength evolution, but

647 instead emphasizes that it is not necessary to invoke an unsteady Burgers rheology when steady-
648 state power-law rheologies can explain the available geodetic observations. As a result, we are
649 tempted to interpret the value of $\hat{n} \geq 3$ in terms of a rheology dominated by dislocation creep,
650 with possible contributions from thermomechanically-coupled processes such as shear heating
651 and grain boundary sliding.

652 4.2.2 Averaging over spatially variable parameters

653 The inferred \hat{A}, \hat{n} values do not only represent averages over multiple physical and chemical pro-
654 cesses, but also over a spatially varying set of parameters. The dominant contribution of this in
655 Equation 12 likely comes from the depth-dependence of temperature i.e., $T(x_3) \propto x_3$. However
656 our ability to geodetically infer spatially varying rheological parameters is limited by the spatial
657 smearing effect of elasticity as well as the apparent homogenization of rheological properties dur-
658 ing shear [e.g., *Hetland and Hager, 2006; Almeida et al., 2018; Ray and Viesca, 2019*]. This implies that
659 we may at best infer a best-fitting \hat{A}, \hat{n} from a single earthquake cycle, with larger events eliciting
660 a response from greater depths and hence a larger $\hat{A} \propto \exp\left(\frac{-Q}{RT}\right)$. The way forward then is to use
661 sequences of earthquakes (events of different magnitudes and/or depth on the same fault), where
662 each individual earthquake may be mapped to a set of uniform \hat{A}, \hat{n} but these parameters show
663 a consistent pattern, such as a fixed \hat{n} but \hat{A} increases with increasing size or depth of the earth-
664 quake. The implication then is that spatial heterogeneity is necessary to explain the observations
665 and therefore we can infer more about how the lithosphere behaves.

666 4.3 Coupling between frictional slip and viscous creep

667 An important implication of mechanically-coupled models of fault slip and distributed deformation,
668 such as our simulations, is that stress-driven interactions between frictional afterslip on the
669 fault and distributed viscous flow in the lower crust and mantle are not independent processes, as
670 is typically considered in many inverse postseismic modeling studies. This simplification explic-
671 itly decouples the mechanical interactions between frictional afterslip and viscous creep and has
672 been shown to systematically bias the location and amplitude of inferred slip and strain [e.g., *Muto*
673 *et al., 2019; Peña et al., 2020*]. Our simulation results suggest that a permissible simplification may
674 be to treat earthquake-driven viscoelastic relaxation as an independent process while afterslip is
675 driven by the coseismic stress change as well as the subsequent viscous flow of the bulk medium.
676 We highlight this by noting the amplitude and temporal evolution of afterslip is markedly dif-
677 ferent between simulations that consider a purely elastic medium versus a viscoelastic medium
678 (Figure 9).

679 4.3.1 Time-dependent loading rate

680 The effect of viscoelastic relaxation on afterslip can be thought of as a modification of the stress
681 loading rate along the fault. For an isolated system, the governing equation for frictional slip in
682 response to a coseismic stress step is $k(v^\infty - v(t)) \propto \frac{df(v(t))}{dt}$ where f is the velocity dependent fric-
683 tion coefficient, k is the elastic stiffness and v^∞ is the long-term slip rate of the fault [*Marone et al.,*
684 *1991*]. When viscoelastic relaxation of the medium is factored in, the loading term now contains
685 two contributions - a time-invariant contribution from v^∞ , and time-dependent stress transfer due
686 to viscous creep in the surrounding medium [*Pollitz, 2017, 2012*]. Viscous creep is itself a decay-
687 ing function in time, with the exact decay rate being a function of the rheology (Figure 3). Thus,

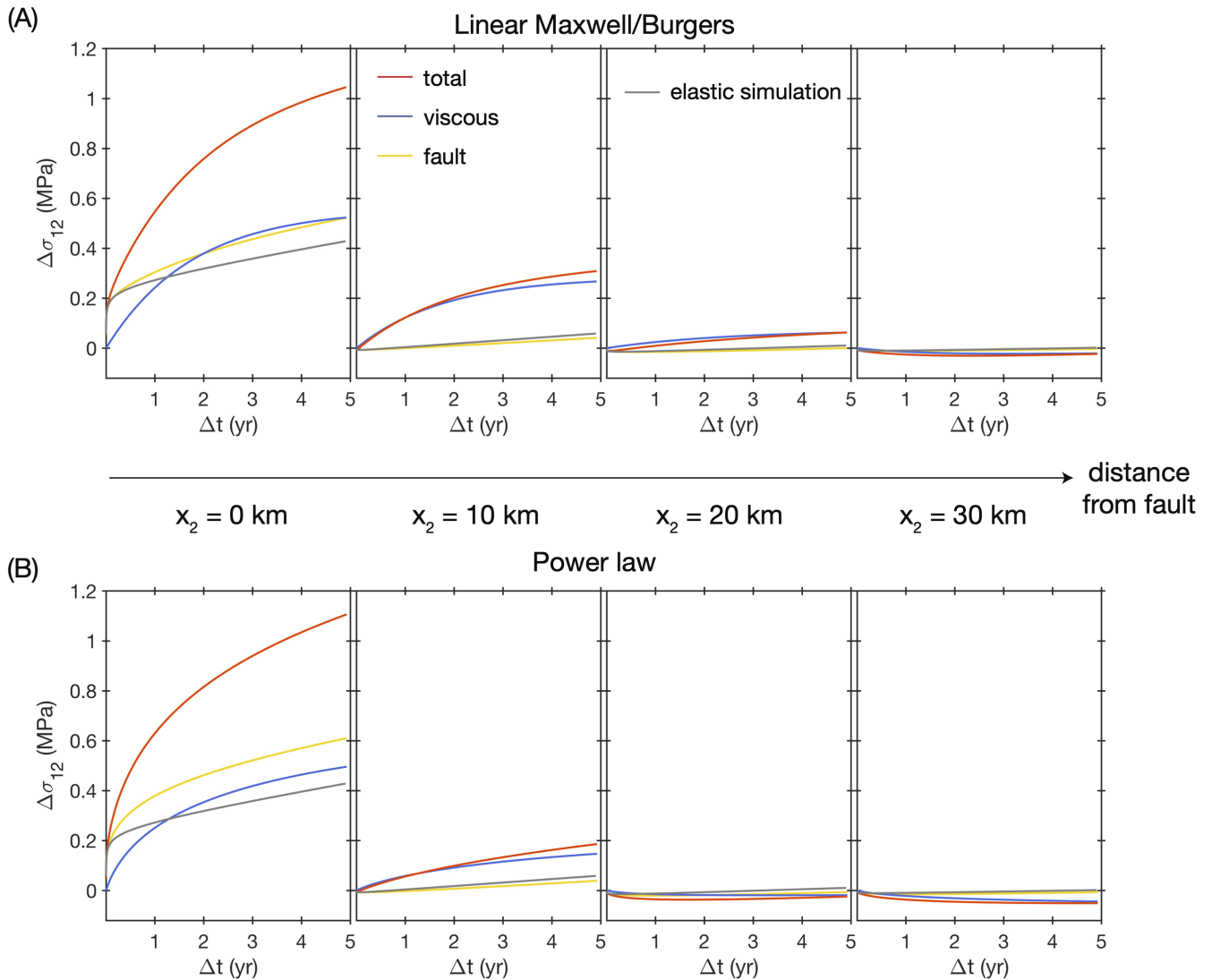


Figure 9: Stress change and decomposition into contributions from fault slip and viscous shear for (A) linear Burgers rheology ($\eta_k = 3 \times 10^{18}$, $\eta_M = 10^{20}$ Pa-s) with effective viscosity $\sim 5 \times 10^{18}$ Pa-s in the plotted time window, and (B) power law rheology with $n = 3, A^{-1} = 10^{19}$. Stress is plotted at 0, 10, 20 and 30 km away from the fault at 10 km depth. Total stress evolution from a nearly elastic model (linear Maxwell simulation with $\eta_M = 10^{20}$ Pa-s) is also shown (gray). The stress evolution over the first 5 years is dominated by the viscoelastic response for linear and power-law rheologies. Additionally, due to the mechanical coupling between fault slip and viscous shear, stress transfer from fault slip evolution in the viscoelastic simulations is significantly different from the elastic simulations.

688 the effective loading rate for afterslip is no longer time-invariant and the resulting timeseries for
689 slip and stress transferred to the surrounding medium can notably differ from simulations that
690 decouple afterslip and viscous creep (Figure 9).

691 4.3.2 Regional stress interactions

692 The difference in time-dependent loading between purely elastic fault models and those consid-
693 ering viscoelastic deformation suggests that viscoelastic interactions are an important ingredient
694 for efforts aimed at modeling regional tectonics and multi-fault interactions, particularly given
695 that the spatial footprint of this distributed deformation can be much larger than that of slip on
696 individual faults (Figure 3-4). Viscoelastic stress interactions have been noted to be relevant to
697 along-strike stress transfer and timing of a recent sequence of great earthquakes on the North
698 Anatolian Fault [Devries and Meade, 2016; Devries et al., 2017], and Southern California [e.g., Freed
699 and Lin, 2001]. More generally, time-dependent loading alters the stress state on the fault preced-
700 ing dynamic rupture. This pre-rupture stress state has been noted to control many aspects of the
701 rupture process from earthquake nucleation to rupture arrest, including the likelihood of ruptures
702 propagating over multiple fault segments [e.g., Zheng and Rice, 1998; Noda et al., 2009; Ulrich et al.,
703 2018; Lambert et al., 2021; Lambert and Lapusta, 2021].

704 Time-dependent loading due to viscous creep may be particularly important when consider-
705 ing interactions between major plate boundary faults and neighboring lower slip rate faults [Freed,
706 2005; Kenner and Simons, 2005]. For low slip rate faults, the loading due to the long-term tectonic
707 loading rate, which is relatively small for low v^∞ , may be overwhelmed by the static stress trans-
708 fer from a nearby earthquake and the corresponding viscous response of the ductile lower crust
709 and mantle (Figure 9). As a result, seismicity on such low slip rate faults may cluster in time
710 with large earthquakes on the major plate boundary fault and may be indicative of coordinated
711 time-dependent loading, as opposed to an individual long-term loading rate of each fault within
712 this system. Future work is needed to develop more realistic treatments of fault loading in larger-
713 scale simulations of fault networks and models of seismic hazard [e.g., Tullis et al., 2012; Shaw et al.,
714 2018], potentially including physically-motivated approximations of viscoelastic contributions to
715 the effective loading rate of fault populations,.

716 5 Conclusions

717 Geodetic recordings of earthquake cycle deformation related to large earthquakes provide geo-
718 scientists with one of the best opportunities to estimate the effective rheology of the lithosphere-
719 asthenosphere system. Data-driven improvements in our estimates of rheological models and
720 relevant parameters translate into better constraints on the dynamics of the earthquake cycle.
721 For classical spring-slider descriptions of the earthquake cycle, a primary assumption is that the
722 long-term loading rate is fixed and deviations from this long-term motion arise from frictional
723 locking and sliding of different sections of the fault. Elasticity is the primary mechanism to trans-
724 fer stress between different locked or sliding fault sections, and since stress in an elastic model
725 decays monotonically from the source, stress interactions between faults are controlled by how
726 far away faults are from each other. The dominant effect of viscoelasticity is to modify how stress
727 is transferred through the medium from one section of fault to another; it alters both, the spatial
728 and temporal pattern of stress evolution compared to purely elastic models. This time-dependent
729 viscoelastic stress transfer invalidates the assumption of a stationary long-term loading rate for
730 a considerable section of the lithosphere surrounding the fault. By altering the effective load-

731 ing rate of the plate boundary system, the viscoelasticity of the lithosphere is a cause for signifi-
732 cantly stronger temporal linkage and long-distance interactions between faults than expected by
733 frictional-elastic models of faults, with significant implications for seismic hazard and risk esti-
734 mates for populations living close to these regions.

735 From our numerical investigations and qualitative comparisons with geodetic observations of
736 the earthquake cycle, we find that the average viscoelastic description of the lithosphere may be
737 that of a power-law spring-dashpot system, although Burgers rheologies may also satisfactorily
738 explain the data but invoke more tunable parameters. Our preferred parameterization of the vis-
739 cious element in this spring-dashpot system follows a steady-state flow law of the form $\dot{\epsilon} = A\sigma^n$,
740 and the parameter ranges for the pre-factor $1/A$ range from $10^{18} - 10^{20}$ and the power exponent
741 $n \geq 3$. The power exponent $n \geq 3$ may strongly hint at dislocation creep being a dominant process
742 throughout the earthquake cycle. However, we caution direct interpretation of these parameters
743 from single earthquake relaxation studies. Further validation from sequences of earthquakes that
744 drive relaxation of the same part of the lithosphere through viscous creep is necessary for us to un-
745 derstand how observational data record the weighted contributions of various micro-mechanical
746 and thermal feedback processes that are active under the hood of this complex dynamical system.

747 Acknowledgements

748 This research was supported by a Texaco Postdoctoral Fellowship awarded to R.M and partly
749 funded by the Earth Observatory of Singapore. V.L. is supported by a National Science Found-
750 ation EAR Postdoctoral Fellowship. The authors are grateful to Roland Bürgmann and Judith
751 Hubbard for discussions and suggestions for this project. No data was used in this study. All the
752 MATLAB code required to recreate the results of this study is available at https://github.com/mallickrishg/viscofric2d_evo.

754 References

- 755 [1] (2020), *A Vision for NSF Earth Sciences 2020-2030*, National Academies Press, Washington,
756 D.C., doi:10.17226/25761.
- 757 [2] Allison, K. L., and E. M. Dunham (2017), Earthquake cycle simulations with rate-and-state
758 friction and power-law viscoelasticity, *Tectonophysics*, (May), 0–1, doi:10.1016/j.tecto.2017.
759 10.021.
- 760 [3] Allison, K. L., and E. M. Dunham (2021), Influence of Shear Heating and Thermomechanical
761 Coupling on Earthquake Sequences and the Brittle-Ductile Transition, *Journal of Geophysical
762 Research: Solid Earth*, 126(6), 1–28, doi:10.1029/2020jb021394.
- 763 [4] Almeida, R., E. O. Lindsey, K. Bradley, J. Hubbard, R. Mallick, and E. M. Hill (2018), Can the
764 Updip Limit of Frictional Locking on Megathrusts be Detected Geodetically? Quantifying
765 the Effect of Stress Shadows on Near-Trench Coupling, *Geophysical Research Letters*, doi:10.
766 1029/2018GL077785.
- 767 [5] Alwahedi, M. A., and J. C. Hawthorne (2019), Intermediate-Magnitude Postseismic Slip
768 Follows Intermediate-Magnitude (M 4 to 5) Earthquakes in California, *Geophysical Research
769 Letters*, 46(7), 3676–3687, doi:10.1029/2018GL081001.

- 770 [6] Avouac, J.-P. (2015), From Geodetic Imaging of Seismic and Aseismic Fault Slip to Dy-
771 namic Modeling of the Seismic Cycle, *Annual Review of Earth and Planetary Sciences*, 43(1),
772 150223150959,000, doi:10.1146/annurev-earth-060614-105302.
- 773 [7] Barbot, S. (2018), Deformation of a Half-Space from Anelastic Strain Confined in a Tetra-
774 hedral Volume, *Bulletin of the Seismological Society of America*, 108(5A), 2687–2712, doi:
775 10.1785/0120180058.
- 776 [8] Bruhat, L., S. Barbot, and J. P. Avouac (2011), Evidence for postseismic deformation of the
777 lower crust following the 2004 Mw6.0 Parkfield earthquake, *Journal of Geophysical Research:*
778 *Solid Earth*, 116(8), 1–10, doi:10.1029/2010JB008073.
- 779 [9] Bürgmann, R., and G. Dresen (2008), Rheology of the Lower Crust and Upper Mantle: Ev-
780 idence from Rock Mechanics, Geodesy, and Field Observations, *Annual Review of Earth and*
781 *Planetary Sciences*, 36(1), 531–567, doi:10.1146/annurev.earth.36.031207.124326.
- 782 [10] Chen, T., and N. Lapusta (2009), Scaling of small repeating earthquakes explained by in-
783 teraction of seismic and aseismic slip in a rate and state fault model, *Journal of Geophysical*
784 *Research: Solid Earth*, 114(1), 1–12, doi:10.1029/2008JB005749.
- 785 [11] Chopra, P. N. (1997), High-temperature transient creep in olivine rocks, *Tectonophysics*,
786 93(111).
- 787 [12] Chopra, P. N., and M. S. Paterson (1981), The experimental deformation of dunite, *Tectono-*
788 *physics*, 78(1-4), 453–473, doi:10.1016/0040-1951(81)90024-X.
- 789 [13] Cohen, S. C., and M. J. Kramer (1984), Crustal deformation, the earthquake cycle, and mod-
790 els of viscoelastic flow in the asthenosphere, *Geophysical Journal International*, 78(3), 735–750,
791 doi:10.1111/j.1365-246X.1984.tb05068.x.
- 792 [14] Devries, P. M., and B. J. Meade (2013), Earthquake cycle deformation in the Tibetan plateau
793 with a weak mid-crustal layer, *Journal of Geophysical Research: Solid Earth*, 118(6), 3101–3111,
794 doi:10.1002/jgrb.50209.
- 795 [15] Devries, P. M., and B. J. Meade (2016), Kinematically consistent models of viscoelastic stress
796 evolution, *Geophysical Research Letters*, 43(9), 4205–4214, doi:10.1002/2016GL068375.
- 797 [16] Devries, P. M., P. G. Krastev, J. F. Dolan, and B. J. Meade (2017), Viscoelastic block models
798 of the North Anatolian fault: A unified earthquake cycle representation of pre- and post-
799 seismic geodetic observations, *Bulletin of the Seismological Society of America*, 107(1), 403–417,
800 doi:10.1785/0120160059.
- 801 [17] Duputel, Z., P. S. Agram, M. Simons, S. E. Minson, and J. L. Beck (2014), Accounting for
802 prediction uncertainty when inferring subsurface fault slip, *Geophysical Journal International*,
803 197(1), 464–482, doi:10.1093/gji/ggt517.
- 804 [18] England, P. C., R. T. Walker, B. Fu, and M. A. Floyd (2013), A bound on the viscosity of
805 the Tibetan crust from the horizontality of palaeolake shorelines, *Earth and Planetary Science*
806 *Letters*, 375, 44–56, doi:10.1016/j.epsl.2013.05.001.
- 807 [19] Freed, A. M. (2005), Earthquake Triggering By Static, Dynamic, and Postseismic Stress
808 Transfer, *Annual Review of Earth and Planetary Sciences*, 33(1), 335–367, doi:10.1146/annurev.
809 earth.33.092203.122505.

- 810 [20] Freed, A. M., and R. Bürgmann (2004), Evidence of power-law flow in the Mojave desert
811 mantle, *Nature*, 430(6999), 548–551, doi:10.1038/nature02784.
- 812 [21] Freed, A. M., and J. Lin (2001), Delayed triggering of the 1999 Hector Mine earthquake by
813 viscoelastic stress transfer, *Nature*, 411(6834), 180–183, doi:10.1038/35075548.
- 814 [22] Freed, A. M., T. Herring, and R. Bürgmann (2010), Steady-state laboratory flow laws alone
815 fail to explain postseismic observations, *Earth and Planetary Science Letters*, 300(1-2), 1–10,
816 doi:10.1016/j.epsl.2010.10.005.
- 817 [23] Freed, A. M., G. Hirth, and M. D. Behn (2012), Using short-term postseismic displacements
818 to infer the ambient deformation conditions of the upper mantle, *Journal of Geophysical Re-*
819 *search: Solid Earth*, 117(1), 1–15, doi:10.1029/2011JB008562.
- 820 [24] Fukuda, J., K. M. Johnson, K. M. Larson, and S. Miyazaki (2009), Fault friction parameters
821 inferred from the early stages of afterslip following the 2003 Tokachi-oki earthquake, *Journal*
822 *of Geophysical Research*, 114(B4), B04,412, doi:10.1029/2008JB006166.
- 823 [25] Goldsby, D. L., and D. L. Kohlstedt (2001), Superplastic deformation of ice: Experimental
824 observations, *Journal of Geophysical Research: Solid Earth*, 106(B6), 11,017–11,030, doi:10.1029/
825 2000jb900336.
- 826 [26] Hansen, L. N., M. E. Zimmerman, and D. L. Kohlstedt (2011), Grain boundary sliding in
827 San Carlos olivine: Flow law parameters and crystallographic-preferred orientation, *Journal*
828 *of Geophysical Research: Solid Earth*, 116(8), 1–16, doi:10.1029/2011JB008220.
- 829 [27] Hawthorne, J. C., M. Simons, and J. P. Ampuero (2016), Estimates of aseismic slip associated
830 with small earthquakes near San Juan Bautista, CA, *Journal of Geophysical Research: Solid*
831 *Earth*, 121(11), 8254–8275, doi:10.1002/2016JB013120.
- 832 [28] Hearn, E. H., and W. R. Thatcher (2015), Reconciling viscoelastic models of postseismic and
833 interseismic deformation: Effects of viscous shear zones and finite length ruptures, *Journal*
834 *of Geophysical Research: Solid Earth*, 120(4), 2794–2819, doi:10.1002/2014JB011361.
- 835 [29] Henriquet, M., J. P. Avouac, and B. G. Bills (2019), Crustal rheology of southern Tibet con-
836 strained from lake-induced viscoelastic deformation, *Earth and Planetary Science Letters*, 506,
837 308–322, doi:10.1016/j.epsl.2018.11.014.
- 838 [30] Hetland, E. A., and B. H. Hager (2005), Postseismic and interseismic displacements near a
839 strike-slip fault: A two-dimensional theory for general linear viscoelastic rheologies, *Journal*
840 *of Geophysical Research: Solid Earth*, 110(10), 1–21, doi:10.1029/2005JB003689.
- 841 [31] Hetland, E. A., and B. H. Hager (2006), The effects of rheological layering on post-seismic
842 deformation, *Geophysical Journal International*, 166(1), 277–292, doi:10.1111/j.1365-246X.
843 2006.02974.x.
- 844 [32] Hirth, G. (2002), 4 Laboratory constraints on the rheology of the upper mantle, *Reviews in*
845 *Mineralogy and Geochemistry*, 51, 97–120, doi:10.1515/9781501509285-008.
- 846 [33] Hirth, G., and D. L. Kohlstedt (2003), Rheology of the Upper Mantle and the Mantle Wedge:
847 a View From the Experimentalists, *Geophysical Monograph Series*, 138, 83–106.

- 848 [34] Hsu, Y.-J., M. SIMONS, J.-P. AVOUAC, J. GALETZKA, K. SIEH, M. CHLIEH, D. NATAW-
849 IDJAJA, L. PRAWIRODIRDJO, and Y. BOCK (2006), Frictional Afterslip Following the 2005
850 Nias-Simeulue Earthquake, Sumatra, *Science*, 312(5782), 1921–1926, doi:10.1126/science.
851 1126960.
- 852 [35] Hussain, E., T. J. Wright, R. J. Walters, D. P. Bekaert, R. Lloyd, and A. Hooper (2018), Con-
853 stant strain accumulation rate between major earthquakes on the North Anatolian Fault,
854 *Nature Communications*, 9(1), 1–9, doi:10.1038/s41467-018-03739-2.
- 855 [36] Ingleby, T., and T. J. Wright (2017), Omori-like decay of postseismic velocities follow-
856 ing continental earthquakes, *Geophysical Research Letters*, 44(7), 3119–3130, doi:10.1002/
857 2017GL072865.
- 858 [37] Johnson, K. M., and P. Segall (2004), Viscoelastic earthquake cycle models with deep stress-
859 driven creep along the San Andreas fault system, *Journal of Geophysical Research B: Solid*
860 *Earth*, 109(10), 1–19, doi:10.1029/2004JB003096.
- 861 [38] Jónsson, S., P. Segall, R. Pedersen, and G. Björnsson (2003), Post-earthquake ground
862 movements correlated to pore-pressure transients, *Nature*, 424(6945), 179–183, doi:10.1038/
863 nature01776.
- 864 [39] Kanamori, H., and E. E. Brodsky (2004), The physics of earthquakes, *Reports on Progress in*
865 *Physics*, 67(8), 1429–1496, doi:10.1088/0034-4885/67/8/R03.
- 866 [40] Karato, S.-I., M. Paterson, and D. Fitzgerald (1986), Rheology of Synthetic Olivine Aggre-
867 gates ' for hot pressing . The Specimens were then sleeve and for temperature is jacket 1)
868 and were hot pressed, *Journal of Geophysical Research*, 91(B8), 8151–8176.
- 869 [41] Kaufmann, G., and F. Amelung (2000), Reservoir-induced deformation and continental rhe-
870 ology in vicinity of Lake Mead, Nevada, *Journal of Geophysical Research: Solid Earth*, 105(B7),
871 16,341–16,358, doi:10.1029/2000JB900079.
- 872 [42] Kelemen, P. B., and G. Hirth (2007), A periodic shear-heating mechanism for intermediate-
873 depth earthquakes in the mantle, *Nature*, 446(7137), 787–790, doi:10.1038/nature05717.
- 874 [43] Kenner, S. J., and P. Segall (2003), Lower crustal structure in northern California: Impli-
875 cations from strain rate variations following the 1906 San Francisco earthquake, *Journal of*
876 *Geophysical Research: Solid Earth*, 108(B1), ETG 5–1–ETG 5–17, doi:10.1029/2001jb000189.
- 877 [44] Kenner, S. J., and M. Simons (2005), Temporal clustering of major earthquakes along indi-
878 vidual faults due to post-seismic reloading, *Geophysical Journal International*, 160(1), 179–194,
879 doi:10.1111/j.1365-246X.2005.02460.x.
- 880 [45] Lambert, V., and S. Barbot (2016), Contribution of viscoelastic flow in earthquake cycles
881 within the lithosphere-asthenosphere system, *Geophysical Research Letters*, 43(19), 10,142–
882 10,154, doi:10.1002/2016GL070345.
- 883 [46] Lambert, V., and N. Lapusta (2021), Resolving simulated sequences of earthquakes and
884 fault interactions: Implications for physics-based seismic hazard assessment, *Journal of*
885 *Geophysical Research: Solid Earth*, 126(10), e2021JB022193, doi:https://doi.org/10.1029/
886 2021JB022193, e2021JB022193 2021JB022193.

- 887 [47] Lambert, V., N. Lapusta, and D. Faulkner (2021), Scale Dependence of Earthquake Rup-
888 ture Prestress in Models With Enhanced Weakening: Implications for Event Statistics and
889 Inferences of Fault Stress, *Journal of Geophysical Research: Solid Earth*, 126(10), 1–29, doi:
890 10.1029/2021JB021886.
- 891 [48] Larsen, C. F., R. J. Motyka, J. T. Freymueller, K. A. Echelmeyer, and E. R. Ivins (2005), Rapid
892 viscoelastic uplift in southeast Alaska caused by post-Little Ice Age glacial retreat, *Earth and*
893 *Planetary Science Letters*, 237(3-4), 548–560, doi:10.1016/j.epsl.2005.06.032.
- 894 [49] Lehner, F. K., and V. C. Li (1982), Large-scale characteristics of plate boundary deforma-
895 tions related to the post-seismic readjustment of a thin asthenosphere, *Geophysical Journal*
896 *International*, 71(3), 775–792, doi:10.1111/j.1365-246X.1982.tb02797.x.
- 897 [50] Li, V. C., and J. R. Rice (1987), Crustal deformation in Great California earthquake cycles,
898 *Journal of Geophysical Research*, 92(B11), 11,533 – 11,551, doi:10.1029/JB092iB11p11533.
- 899 [51] Lyzenga, G. A., A. Raefsky, and S. G. Mulligan (1991), Models of recurrent strike-slip earth-
900 quake cycles and the state of crustal stress, *Journal of Geophysical Research: Solid Earth*,
901 96(B13), 21,623–21,640, doi:10.1029/91JB02260.
- 902 [52] Mallick, R., R. Bürgmann, K. Johnson, and J. Hubbard (2021), A Unified Framework for
903 Earthquake Sequences and the Growth of Geological Structure in Fold-Thrust Belts, *Journal*
904 *of Geophysical Research: Solid Earth*, 126(9), 1–26, doi:10.1029/2021JB022045.
- 905 [53] Marone, C. (1998), Laboratory-Derived Friction Laws and Their Application To Seismic
906 Faulting, *Annual Review of Earth and Planetary Sciences*, 26(1), 643–696, doi:10.1146/annurev.
907 earth.26.1.643.
- 908 [54] Marone, C., C. H. Scholz, and R. Bilham (1991), On the mechanics of earthquake afterslip,
909 *Journal of Geophysical Research*, 96(B5), 8441–8452.
- 910 [55] Meade, B. J., Y. Klinger, and E. A. Hetland (2013), Inference of multiple earthquake-cycle
911 relaxation timescales from irregular geodetic sampling of interseismic deformation, *Bulletin*
912 *of the Seismological Society of America*, 103(5), 2824–2835, doi:10.1785/0120130006.
- 913 [56] Milne, G. A., J. L. Davis, J. X. Mitrovica, H. G. Scherneck, J. M. Johansson, M. Vermeer, and
914 H. Koivula (2001), Space-geodetic constraints on glacial isostatic adjustment in fennoscan-
915 dia, *Science*, 291(5512), 2381–2385, doi:10.1126/science.1057022.
- 916 [57] Minson, S. E., M. Simons, and J. L. Beck (2013), Bayesian inversion for finite fault earthquake
917 source models I-theory and algorithm, *Geophysical Journal International*, 194(3), 1701–1726,
918 doi:10.1093/gji/ggt180.
- 919 [58] Montési, L. G. (2004), Controls of shear zone rheology and tectonic loading on postseismic
920 creep, *Journal of Geophysical Research: Solid Earth*, 109(10), doi:10.1029/2003JB002925.
- 921 [59] Montési, L. G., and G. Hirth (2003), Grain size evolution and the rheology of ductile shear
922 zones: From laboratory experiments to postseismic creep, *Earth and Planetary Science Letters*,
923 211(1-2), 97–110, doi:10.1016/S0012-821X(03)00196-1.
- 924 [60] Moore, J. D., and B. Parsons (2015), Scaling of viscous shear zones with depth-dependent
925 viscosity and power-law stress-strain-rate dependence, *Geophysical Journal International*,
926 202(1), 242–260, doi:10.1093/gji/ggv143.

- 927 [61] Moore, J. D. P., H. Yu, C.-H. Tang, T. Wang, S. Barbot, D. Peng, S. Masuti, J. Dauwels, Y.-J.
928 Hsu, V. Lambert, P. Nanjundiah, S. Wei, E. Lindsey, L. Feng, and B. Shibazaki (2017), Imag-
929 ing the distribution of transient viscosity after the 2016 M w 7.1 Kumamoto earthquake,
930 *Science*, 356(6334), 163–167, doi:10.1126/science.aal3422.
- 931 [62] Müller, G. (1986), Generalized Maxwell bodies and estimates of mantle viscosity, *Geophys-*
932 *ical Journal of the Royal Astronomical Society*, 87(3), 1113–1141, doi:10.1111/j.1365-246X.1986.
933 tb01986.x.
- 934 [63] Mulyukova, E., and D. Bercovici (2019), The Generation of Plate Tectonics From Grains to
935 Global Scales: A Brief Review, *Tectonics*, 38(12), 4058–4076, doi:10.1029/2018TC005447.
- 936 [64] Muto, J., J. D. P. Moore, S. Barbot, T. Iinuma, Y. Ohta, and H. Iwamori (2019), Coupled
937 afterslip and transient mantle flow after the 2011 Tohoku earthquake, *Science Advances*, (2),
938 1–9.
- 939 [65] Noda, H., E. M. Dunham, and J. R. Rice (2009), Earthquake ruptures with thermal weak-
940 ening and the operation of major faults at low overall stress levels, *Journal of Geophysical*
941 *Research: Solid Earth*, 114(7), 1–27, doi:10.1029/2008JB006143.
- 942 [66] Peltzer, G., P. Rosen, F. Rogez, and K. Hudnut (1998), Poroelastic rebound along the Lan-
943 ders 1992 earthquake surface rupture, *Journal of Geophysical Research: Solid Earth*, 103(B12),
944 30,131–30,145, doi:10.1029/98jb02302.
- 945 [67] Peña, C., O. Heidbach, M. Moreno, J. Bedford, M. Ziegler, A. Tassara, and O. Oncken (2020),
946 Impact of power-law rheology on the viscoelastic relaxation pattern and afterslip distribu-
947 tion following the 2010 Mw 8.8 Maule earthquake, *Earth and Planetary Science Letters*, 542,
948 116,292, doi:10.1016/j.epsl.2020.116292.
- 949 [68] Perfettini, H., and J.-P. P. Ampuero (2008), Dynamics of a velocity strengthening fault re-
950 gion: Implications for slow earthquakes and postseismic slip, *Journal of Geophysical Research*,
951 113(B9), B09,411, doi:10.1029/2007JB005398.
- 952 [69] Perfettini, H., and J.-P. Avouac (2004), Stress transfer and strain rate variations during
953 the seismic cycle, *Journal of Geophysical Research: Solid Earth*, 109(B6), 1–8, doi:10.1029/
954 2003JB002917.
- 955 [70] Perfettini, H., and J.-P. Avouac (2004), Postseismic relaxation driven by brittle creep: A
956 possible mechanism to reconcile geodetic measurements and the decay rate of aftershocks,
957 application to the Chi-Chi earthquake, Taiwan, *Journal of Geophysical Research: Solid Earth*,
958 109(B2), 1–15, doi:10.1029/2003JB002488.
- 959 [71] Pollitz, F. F. (2005), Transient rheology of the upper mantle beneath central Alaska inferred
960 from the crustal velocity field following the 2002 Denali earthquake, *Journal of Geophysical*
961 *Research: Solid Earth*, 110(8), 1–16, doi:10.1029/2005JB003672.
- 962 [72] Pollitz, F. F. (2012), ViscoSim earthquake simulator, *Seismological Research Letters*, 83(6), 979–
963 982, doi:10.1785/0220120050.
- 964 [73] Pollitz, F. F. (2017), A note on adding viscoelasticity to earthquake simulators, *Bulletin of the*
965 *Seismological Society of America*, 107(1), 468–474, doi:10.1785/0120160192.

- 966 [74] Pollitz, F. F. (2019), Lithosphere and shallow asthenosphere rheology from observations of
967 post-earthquake relaxation, *Physics of the Earth and Planetary Interiors*, 293(November 2018),
968 106,271, doi:10.1016/j.pepi.2019.106271.
- 969 [75] Post, R. L. (1977), High-temperature creep of Mt. Burnet Dunite, *Tectonophysics*, 42(2-4), 75–
970 110, doi:10.1016/0040-1951(77)90162-7.
- 971 [76] Raj, R., and M. F. Ashby (1971), On grain boundary sliding and diffusional creep, *Metallur-
972 gical Transactions*, 2(4), 1113–1127, doi:10.1007/BF02664244.
- 973 [77] Ray, S., and R. C. Viesca (2019), Homogenization of fault frictional properties, *Geophysical
974 Journal International*, 219(2), 1203–1211, doi:10.1093/gji/ggz327.
- 975 [78] Reches, Z., G. Schubert, and C. Anderson (1994), Modeling of periodic great earthquakes on
976 the San Andreas Fault: effects of nonlinear crustal rheology, *Journal of Geophysical Research*,
977 99(B11), 983–1000, doi:10.1029/94jb00334.
- 978 [79] Rutter, E., and K. Brodie (2004), Experimental grain size-sensitive flow of hot-pressed Brazil-
979 ian quartz aggregates, *Journal of Structural Geology*, 26(11), 2011–2023, doi:10.1016/j.jsg.2004.
980 04.006.
- 981 [80] Ryder, I., B. Parsons, T. J. Wright, and G. J. Funning (2007), Post-seismic motion following
982 the 1997 Manyi (Tibet) earthquake: InSAR observations and modelling, *Geophysical Journal
983 International*, 169(3), 1009–1027, doi:10.1111/j.1365-246X.2006.03312.x.
- 984 [81] Savage, J., and J. Svarc (2009), Postseismic relaxation following the 1992 m7. 3 landers and
985 1999 m7. 1 hector mine earthquakes, southern california, *Journal of Geophysical Research: Solid
986 Earth*, 114(B1).
- 987 [82] Savage, J. C. (2000), Viscoelastic-coupling model for the earthquake cycle driven from be-
988 low, *Journal of Geophysical Research*, 105(B11), 25,525, doi:10.1029/2000JB900276.
- 989 [83] Savage, J. C., and R. O. Burford (1973), Geodetic determination of relative plate motion in
990 central California., *Journal of Geophysical Research*, 78(5), 832–845.
- 991 [84] Savage, J. C., and W. H. Prescott (1978), Asthenosphere readjustment and the earth-
992 quake cycle, *Journal of Geophysical Research: Solid Earth*, 83(B7), 3369–3376, doi:10.1029/
993 jb083ib07p03369.
- 994 [85] Savage, J. C., J. L. Svarc, W. Prescott, and K. W. Hudnut (1998), Deformation following the
995 1994 northridge earthquake (m= 6.7), southern california, *Geophysical research letters*, 25(14),
996 2725–2728.
- 997 [86] Scholz, C. H. (1998), Earthquakes and friction laws, *Nature*, 391, 37–42, doi:10.1038/34097.
- 998 [87] Scholz, C. H. (2002), *The Mechanics of Earthquakes and Faulting*, 3.
- 999 [88] Segall, P. (2010), *Earthquake and Volcano Deformation*, 517 pp., Princeton University Press,
1000 Princeton, doi:10.1515/9781400833856.
- 1001 [89] Shaw, B. E., K. R. Milner, E. H. Field, K. Richards-Dinger, J. J. Gilchrist, J. H. Dieterich,
1002 and T. H. Jordan (2018), A physics-based earthquake simulator replicates seismic hazard
1003 statistics across California, *Science Advances*, 4(8), 1–10, doi:10.1126/sciadv.aau0688.

- 1004 [90] Spence, D. A., and D. L. Turcotte (1979), Viscoelastic Relaxation of Cyclic Displacements on
1005 the San Andreas Fault, *Proceedings of the Royal Society of London. A. Mathematical and Physical*
1006 *Sciences*, 365(1720), 121–144.
- 1007 [91] Takeuchi, C. S., and Y. Fialko (2012), Dynamic models of interseismic deformation and stress
1008 transfer from plate motion to continental transform faults, *Journal of Geophysical Research:*
1009 *Solid Earth*, 117(B5), n/a–n/a, doi:10.1029/2011JB009056.
- 1010 [92] Takeuchi, C. S., and Y. Fialko (2013), On the effects of thermally weakened ductile shear
1011 zones on postseismic deformation, *Journal of Geophysical Research: Solid Earth*, 118(12), 6295–
1012 6310, doi:10.1002/2013JB010215.
- 1013 [93] Tamisiea, M. E., J. X. Mitrovica, and J. L. Davis (2007), GRACE Gravity Data Constrain
1014 Ancient Ice Geometries and Continental Dynamics over Laurentia, *Science*, 316(5826), 881–
1015 883, doi:10.1126/science.1137157.
- 1016 [94] Tang, C.-H., Y.-J. Hsu, S. Barbot, J. D. P. Moore, and W.-L. Chang (2019), Lower-crustal
1017 rheology and thermal gradient in the Taiwan orogenic belt illuminated by the 1999 Chi-Chi
1018 earthquake, *Science Advances*, 5(2), eaav3287, doi:10.1126/sciadv.aav3287.
- 1019 [95] Tarantola, A. (2006), Popper, Bayes and the inverse problem, *Nature Physics*, 2(8), 492–494,
1020 doi:10.1038/nphys375.
- 1021 [96] Tullis, T. E., K. Richards-Dinger, M. Barall, J. H. Dieterich, E. H. Field, E. M. Heien,
1022 L. H. Kellogg, F. F. Pollitz, J. B. Rundle, M. K. Sachs, D. L. Turcotte, S. N. Ward, and
1023 M. B. Yikilmaz (2012), A comparison among observations and earthquake simulator re-
1024 sults for the allcal2 California fault model, *Seismological Research Letters*, 83(6), 994–1006,
1025 doi:10.1785/0220120094.
- 1026 [97] Ulrich, T., A.-A. Gabriel, J.-P. Ampuero, and W. Xu (2018), Dynamic viability of the 2016
1027 Mw 7.8 Kaikōura earthquake cascade on weak crustal faults, *Nature Communications*, (2019),
1028 doi:10.31223/OSF.IO/AED4B.
- 1029 [98] Vernant, P. (2015), What can we learn from 20years of interseismic GPS measurements across
1030 strike-slip faults?, *Tectonophysics*, 644, 22–39, doi:10.1016/j.tecto.2015.01.013.
- 1031 [99] Wang, K., and Y. Fialko (2018), Observations and modeling of coseismic and postseismic de-
1032 formation due to the 2015 mw 7.8 gorkha (nepal) earthquake, *Journal of Geophysical Research:*
1033 *Solid Earth*, 123(1), 761–779.
- 1034 [100] Wen, Y., Z. Li, C. Xu, I. Ryder, and R. Bürgmann (2012), Postseismic motion after the 2001
1035 mw 7.8 kokoxili earthquake in tibet observed by insar time series, *Journal of geophysical re-*
1036 *search: solid earth*, 117(B8).
- 1037 [101] Wimpenny, S., A. Copley, and T. Ingleby (2017), Fault mechanics and post-seismic deforma-
1038 tion at bam, se iran, *Geophysical Journal International*, 209(2), 1018–1035.
- 1039 [102] Yamashita, F., E. Fukuyama, K. Mizoguchi, S. Takizawa, S. Xu, and H. Kawakata (2015),
1040 Scale dependence of rock friction at high work rate, *Nature*, 528(7581), 254–257, doi:10.1038/
1041 nature16138.

- 1042 [103] Zhao, D., C. Qu, R. Bürgmann, W. Gong, and X. Shan (2021), Relaxation of Tibetan Lower
1043 Crust and Afterslip Driven by the 2001 Mw7.8 Kokoxili, China, Earthquake Constrained by
1044 a Decade of Geodetic Measurements, *Journal of Geophysical Research: Solid Earth*, 126(4), 1–33,
1045 doi:10.1029/2020JB021314.
- 1046 [104] Zheng, G., and J. R. Rice (1998), Conditions under which velocity-weakening friction al-
1047 lows a self-healing versus a cracklike mode of rupture, *Bulletin of the Seismological Society of*
1048 *America*, 88(6), 1466–1483.